J. Fluid Mech. (2007), *vol.* 577, *pp.* 467–494. © 2007 Cambridge University Press
doi:10.1017/S0022112007004764 Printed in the United Kingdom

Liquid sloshing and wave breaking in circular and square-base cylindrical containers

A. ROYON-LEBEAUD†, E. J. HOPFINGER AND A. CARTELLIER

LEGI, CNRS/INPG, UJFBP 53, 38041, Grenoble Cedex, France

(Received 27 February 2006 and in revised form 2 November 2006)

Near resonance sloshing in containers, filled with a liquid to a given depth h, depends on three parameters, which are the viscous damping, the frequency offset that contains the forcing amplitude and the fluid depth. Experiments have been conducted with low-viscosity liquids mainly in circular cylindrical containers of radius R subjected to harmonic horizontal forcing; complementary experiments on wave breaking have been performed in a square-base container. The fluid depth was kept large ($h/R > 1$) so that it was no longer a variable parameter. The bounds of existence of the different wave regimes, namely planar waves, swirling waves, chaotic sloshing as well as breaking waves, have been determined as a function of forcing frequencies relative to the lowest natural frequency ω_1 and for a wide range of forcing amplitudes. It is shown that when the forcing frequency ω is slightly larger than the lowest natural frequency ω_1, planar wave motion bifurcates to a swirling wave mode at finite wave amplitude, the value of which depends on the offset parameter. The swirl wave amplitude grows exponentially and saturates at a certain value. The swirl has a hard-spring behaviour, is very robust and can generate a vortical flow of the liquid column. Chaotic sloshing and wave breaking occur quasi-periodically: growth of planar wave amplitude at a rate depending on the forcing amplitude, collapse, irregular swirl and again growth of planar wave amplitude. The details and periodicity of the chaotic behaviour and breaking depend on the frequency-offset parameter. Close to the natural frequency, chaotic wave motion is possible without breaking. Planar wave breaking is, in general, associated with spilling caused by the encounter of nearly freely falling lumps of fluid with the upward moving wave crest, in a way demonstrated previously in two-dimensional wave breaking. In three dimensions, the wave crest is destabilized in the crosswise direction so that spilling is not uniform along the wave crest and an irregular swirl is generated following breaking; free fall of fluid lumps occurs over many wave periods. The complementary experiments, performed in a square-base container of base dimension L, show four different wave patterns of wavelengths L and $L/2$ crosswise to the primary wave. This cross-wave instability is interpreted in terms of parametric instability.

1. Introduction

Liquid sloshing in storage tanks is a fundamental problem, related to nonlinear oscillators and dynamic systems (Miles 1984*b*; Bridges 1987; Funakoshi & Inoue 1988). It is also of considerable practical importance as it can lead to accidents due

† Present address: IFP Lyon, BP 31, 69390 Vernaison, France.

https://doi.org/10.1017/S0022112007004764 Published online by Cambridge University Press

to the forces exerted on the container walls and possible large pressure changes due to evaporation or condensation. Ibrahim (2005) gives a detailed summary of the theory and fundamentals of sloshing under widely different conditions, and contains approximately three thousand references. Abramson in his foreword to this book mentions that nonlinear sloshing can be bewildering in its complexity. During the early development of space flights, liquid sloshing in fuel tanks received considerable attention (Abramson 1966). The sloshing wave modes have been analysed in detail for containers of various geometries, including nonlinear sloshing and geometric effects on the damping of the liquid motion. Most of the time the containers are subjected to lateral forcing, giving rise to asymmetric gravity wave motions. Vertical forcing, parallel to the container axis, is also encountered which generates symmetric or asymmetric wave modes (depending on forcing frequency) known as parametric or Faraday instability. In a circular cylindrical container, as well as in square-base containers, large-amplitude asymmetric waves bifurcate to a swirling wave motion at forcing frequencies near and above the natural frequency depending on forcing amplitude (Abramson, Chu & Dodge 1966; Miles 1984*b*; Faltinsen, Rognebakke & Timokha 2003, 2005). Furthermore, the fluid depth is an important parameter because resonant waves have a negative or positive nonlinearity, depending on the liquid fill ratio (Miles 1984*a*; Waterhouse 1994; Faltinsen *et al.* 2003). In square-base containers and at small fluid depths, secondary frequency bifurcations are possible (Bridges 1987). The modal theory developed by Faltinsen *et al.* (2000, 2003, 2006) and applied to rectangular and square-base containers is very powerful and allows the calculation of the stability limits of stable nonlinear waves for different fill ratios as well as the forces and moments exerted on the tank walls. Hutton (1963) used a Taylor expansion of the surface displacement and Miles (1976, 1984*b*) developed a Lagrangian–Hamiltonian formulation to treat weakly nonlinear sloshing in circular cylinders.

Experimentally, different aspects of sloshing have been considered. Hutton (1963) compared his theoretical stability boundaries with experiments. The predicted results were found to agree well with experiments for planar waves, but poorly for swirling waves. The most detailed experiments, giving the bounds of the different wave regimes, are those of Abramson *et al.* (1966). However, these experiments also raise questions about the domain of existence of a swirling wave mode. Furthermore, Hutton (1964) and Faller (1983, 2001) demonstrated that large-amplitude swirling waves generate a vortical flow of the liquid column that enlarges the frequency range of existence of this wave mode owing to a Doppler shift. Funakoshi & Inoue (1988) examined the transitions from planar waves to chaos and swirling waves in terms of dynamical systems theory.

Little is known about the three-dimensional wave-breaking conditions of standing waves. Jiang, Perlin & Schultz (1998) showed a period tripling scenario of two-dimensional standing-wave breaking. Experiments on wave breaking by Bredmose *et al.* (2003) in a rectangular tank of length to width equal to 3.7, subjected to horizontal forcing, showed the existence of table-top breakers with relatively long periods of free fall. These experiments give some guidance for fully three-dimensional breaking in cylindrical and square-base containers, but there are important differences, essentially because of the existence of two conjugate wave modes. Taylor (1953) discusses three-dimensional breaking of standing waves in a rectangular container and some experimental results on breaking of waves in a square-base container are presented by Faltinsen *et al.* (2003). Capillary wave breaking described by James, Smith

https://doi.org/10.1017/S0022112007004764 Published online by Cambridge University Press

& Glezer (2003) is also encountered in the final stage of breaking when ligaments form.

Here we present new experimental results on large-amplitude sloshing and wave breaking in circular cylindrical containers. In order to illustrate more clearly the basic three-dimensional wave-breaking scenarios, complementary experiments have been conducted in a square-base container. Image analysis and local measurements (by capacitance probes) of the wave amplitude were used to determine the steady-state wave motions as well as the transients and chaos up to breaking and beyond. The effect of viscous damping is very small in the sense of Miles (1984*b*). In § 2, some useful theoretical concepts, with emphasis on Miles' (1984*b*) weakly nonlinear theory, are presented. Section 3 contains a description of the experimental configuration and procedures. In § 4, the different steady-state wave regimes (amplitude response curves) are discussed, and § 5 contains the bifurcations and transients. Chaos and resonant breaking conditions are presented in § 6, and in § 7 planar wave breaking in a square-base container is illustrated. Concluding discussions are presented in § 8.

2. Theoretical background

2.1. *Normal modes*

The wave motion of an inviscid incompressible fluid in a rigid tank is governed by the free-boundary potential flow equations presented in a large number of publications (see for instance Abramson 1966; Faltinsen *et al.* 2003; Ibrahim 2005). For a circular cylinder, the velocity potential of the free-boundary fluid motion relative to the container satisfies the (linear) Laplace equation. Its solution is of the form (Ibrahim 2005):

$$\phi(r,\theta,z,t) = [\alpha_{mn}(t)\cos m\theta + \beta_{mn}(t)\sin m\theta]J_m(k_{mn}r)\frac{\cosh(k_{mn}(z+h)}{\cosh(k_{mn}h)} \quad (m=0,1,\ldots,n=1,2,\ldots), \quad (1)$$

where z is measured upward from the undisturbed free surface in the cylindrical polar coordinate system (θ, r, z), h is the fluid depth, $J_m(k_{mn}r)$ a Bessel function and $\alpha_{mn}(t)$ and $\beta_{mn}(t)$ are time-dependent coefficients which can be expressed in terms of harmonic functions $\sin\omega_{mn}t$. The free-surface elevation and natural frequency are, respectively, obtained from the linearized free-surface boundary condition $\dot{\phi} - g\eta = 0$ and from $\ddot{\phi} + g\partial\phi/\partial z = 0$. The free-surface elevation reads:

$$\eta(r,\theta,t) = [A_{mn}\cos m\theta + B_{mn}\sin m\theta]J_m(k_{mn}r)\cos\omega_{mn}t \quad (m=0,1,\ldots,n=1,2\ldots), \quad (2)$$

where A_{mn} and B_{mn} contain gravity g. The natural frequency, when adding surface tension, is:

$$\omega_{mn}^2 = gk_{mn}\left(1+\frac{k_{mn}^2\sigma}{g\rho}\right)\tanh(k_{mn}h). \quad (3)$$

The boundary condition on the container wall is $\partial\phi/\partial r|_{r=R} = J_m'(k_{mn}R) = 0$ which gives for the axisymmetric modes, up to $n=2$, $k_{01}R = 3.832$ and $k_{02}R = 7.015$ and for the asymmetric modes $k_{11}R = 1.841$ and $k_{12}R = 5.335$. The corresponding natural frequencies are given by (3). The two dominant asymmetric modes of free-surface oscillation of wavenumber $k_{11}R = 1.841$, have thus the same frequency $\omega_{11} \equiv \omega_1$ and, according to (2), differ only by an azimuthal rotation $\pi/2$. These two dominant modes are linearly orthogonal, but are coupled at third order in wave amplitude.

https://doi.org/10.1017/S0022112007004764 Published online by Cambridge University Press

Viscous effects have been neglected in the foregoing theoretical development. The natural frequency shift due to linear damping is $\widehat{\omega}_{mn} = \omega_{mn}(1-\delta)$ where $\delta = \kappa/\omega_{mn}$ is the damping ratio and κ the damping rate. In general, there is viscous dissipation in the Stokes boundary layers and in the bulk. The respective contributions are (Lighthill 1978) $\delta \sim (1/R)(\nu/2\omega_{mn})^{1/2} + (1/R^2)(2\nu/\omega_{mn})$. The weighting factors depend on the wave modes. For low viscosity fluids (small ν) and sufficiently large containers, the bulk dissipation is an order of magnitude smaller than dissipation at the boundaries (Miles & Henderson 1998). For dissipation at the boundaries, Henderson & Miles (1990) give the following analytical expression:

$$\delta = \frac{1}{2R}\left(\frac{\nu}{2\omega_{mn}}\right)^{1/2}\left[\frac{2k_{mn}R}{\sinh 2k_{mn}h} + \frac{2k_{mn}R\cosh^2 k_{mn}h}{\sinh 2k_{mn}h} + \frac{1+(m/k_{mn}R)^2}{1-(m/k_{mn}R)^2} - \frac{2k_{mn}h}{\sinh 2k_{mn}h}\right]. \tag{4}$$

The first and second terms in square brackets represent damping at the bottom and at the free surface and the last two terms correspond to damping at the side boundaries. For deep water and a free surface without rigidity, this expression reduces to

$$\delta = \frac{1}{2R}\left(\frac{\nu}{2\omega_{mn}}\right)^{1/2}\frac{1+(m/k_{mn}R)^2}{1-(m/k_{mn}R)^2}. \tag{5}$$

Using the dispersion relation (3) and neglecting surface tension terms, (5) can be written in the form

$$\delta = C_1(\nu^2/R^3 g)^{1/4}, \tag{6}$$

where the coefficient C_1 is a function of the wave mode as indicated by (5). For the lowest asymmetric mode, $k_{11}R = 1.841$, experiments give $0.8 \leqslant C_1 \leqslant 1.4$ (Silverman & Abramson 1966; Royon-Lebeaud 2005). This is a factor of about 2 larger than predicted by (5). A similar difference between theoretical and experimental damping ratios has been observed by Henderson & Miles (1990) for other wave modes.

2.2. *Weakly nonlinear theories*

Hutton (1963) developed the velocity potential and free-surface displacement to third order for nonlinear waves in a circular cylinder subjected to horizontal harmonic forcing. He was able to establish the third-order coupling between the primary modes and show that planar resonant wave motion is unstable in a certain neighbourhood of the natural frequency and that the nonlinearly coupled motion, causing swirl, is stable. Miles (1976) established the Lagrangian and Hamiltonian for nonlinear gravity-wave motion in a rectangular container in terms of generalized coordinates of the free-surface displacement. Miles (1984*a*) extended this formulation to weakly nonlinear free sloshing in a circular cylinder and then (Miles 1984*b*) to weakly nonlinear surface wave motions when the container is subjected to horizontal harmonic forcing near the resonance frequency of the primary modes. It is useful to summarize this theory because it contains the relevant control parameters, gives the amplitude response curve with the bifurcation points and provides physical insight into the amplitude-frequency response. Miles (1984*b*) poses

$$\eta(r,\theta,t) = \eta_n(t)\psi_n(r,\theta) \quad (n = 1, 2, \ldots), \tag{7}$$

where $\eta_n(t)$ are generalized coordinates and $\psi_n(r,\theta)$ are the normal modes given by

$$\psi_n \equiv \psi_{mn}^{c,s} = \frac{J_m(k_{mn}r)}{N_{mn}}(\cos m\theta, \sin m\theta) \quad (m = 0, 1, \ldots,\ n = 1, 2, \ldots), \tag{8}$$

https://doi.org/10.1017/S0022112007004764 Published online by Cambridge University Press

where $N_{mn}^2 = [1 - (m/k_{mn}R)^2]J_m^2(k_{mn}R)/2$. In this notation, the two normal primary modes of wave number $k_{11} \equiv k_1$ are given by

$$\psi_{1,2} \equiv \psi_{11}^{c,s} = N^{-1} J_1(k_1 r)(\cos\theta, \sin\theta), \tag{9}$$

where $N \equiv N_{11} = 0.345$ and superscripts c, s stand for $\cos\theta$ and $\sin\theta$. When the container is forced horizontally by the x-directed (in the $\theta = 0$ plane) displacement $x = A_f \cos\omega t$, the external force potential to be included in the Lagrangian is of the form $\omega^2 A_f x_1 \eta_1$, where $x_1 = 0.4986R$ when ω is near the dominant modes $m = n = 1$. The Lagrangian, truncated at fourth order in $\eta_n(t)$, has general solutions of the form:

$$\eta_n = \varepsilon\ell\{p_n(\tau)\cos\omega t + q_n(\tau)\sin\omega t\} \quad (n = 1, 2), \tag{10}$$

for the two primary modes and

$$\eta_n = \varepsilon^2\ell\{A_n(\tau)\cos 2\omega t + B_n(\tau)\sin 2\omega t + C_n(\tau)\} \quad (n \neq 1, 2), \tag{11}$$

for the secondary modes. For planar waves, $p_2 = q_2 = 0$, whereas the surface displacement of non-planar waves is composed of amplitudes of subscript $n = 1$ and 2. The coefficients p_n, q_n, A_n, B_n and C_n are slowly varying dimensionless amplitudes which depend on the slow, dimensionless time scale $\tau = (\varepsilon^2\omega t)/2$. The parameters in equations (10) and (11) are:

$$\ell = \frac{R}{1.841}\tanh(1.841h/R), \qquad \varepsilon^3 = 1.684\frac{A_f}{R}, \tag{12}$$

where ε is a small parameter, $0 < \varepsilon \ll 1$. Consistency of the Lagrangian, truncated at fourth-order, requires that all the terms are $O(\varepsilon^4)$. Therefore, the forcing term $F_1 \propto A_f\omega^2 = O(\varepsilon^3)$, quadratic terms in η_1 and η_2, that force non-resonant secondary modes, are $O(\varepsilon^2)$ and frequency offset $\omega^2 - \omega_1^2 = O(\varepsilon^2\omega_1^2)$. This introduces the frequency offset parameter in the form

$$\beta = \frac{\omega^2 - \omega_1^2}{\varepsilon^2\omega_1^2}. \tag{13}$$

Substitution of (10) and (11) into the expression of the Lagrangian and averaging over a 2π interval of ωt leads to the average Lagrangian which contains a constant of the motion, namely the Hamiltonian H. The canonical equations give the evolution equations of the amplitudes of the primary modes $\dot{p}_n$ and $\dot{q}_n$ where overdots represent differentiation with respect to τ. Linear damping can be added to the canonical equations in the form $-\alpha(p_n, q_n)$ where

$$\alpha = 2\delta/\varepsilon^2, \tag{14}$$

and δ the damping ratio (6). Weakly nonlinear wave motion is, therefore, governed by four evolution equations (ODE) of $\dot{p}_1$, $\dot{q}_1$, $\dot{p}_2$, $\dot{q}_2$ containing three control parameters, α, β and ℓ (i.e. h/R). The fixed points (steady-state resonance curves) and bifurcation points where the number of fixed points changes, are obtained from the steady-state solutions of these equations. For small α there are five bifurcation points β_i, $i = 1$, 2, 3, 4, 5 (or 6), the values of which depend on h/R through the parameters A and B determined by Miles (1984*a*).

Miles (1984*b*) and Funakoshi & Inoue (1988) studied in detail this dynamic system of four ordinary differential equations (ODE) with three control parameters. The bifurcation points β_1 and β_2 are shown to be Hopf bifurcation points, but when $\alpha^2 \ll 1$, only β_2 exists. The resonantly forced spherical pendulum (Miles 1984*c*) corresponds to particular values of A and B. If secondary modes were not excited at

https://doi.org/10.1017/S0022112007004764 Published online by Cambridge University Press

second order in η_1 and η_2, weakly nonlinear sloshing would be fully analogous to the motion of a spherical pendulum. In deep water, the contribution of the two primary modes represents about 65 % of the kinetic energy (Gavrilyuk, Lukovsky & Timokha 2000). These authors solved numerically a five-mode (two primary modes and three secondary modes) model equation for sloshing in a circular cylinder subjected to harmonic horizontal forcing.

Of interest also are the amplitude corrections of the resonance frequency in terms of the parameters A and B (Miles 1984*a*). The expression for planar waves is of the form

$$\frac{\omega}{\omega_1} = 1 - \tfrac{1}{2}A\frac{\overline{\eta^2}}{\ell^2}, \tag{15}$$

where $\overline{\eta^2}$ is the mean square of the free-surface displacement. The sign and magnitude of the parameter A changes with liquid depth. For a deep fluid layer, $h/R \gg 1$, A is positive ($A = 1.11$) and the first asymmetric mode has a negative nonlinearity (soft spring behaviour). This means that resonance of the nonlinear system is observed at a frequency lower than the linear natural frequency of the first natural mode. Taylor (1953), in his experiments with standing waves, clearly demonstrated this negative nonlinearity. A changes sign at $h/R = 0.506$ and goes to minus infinity at $h/R = 0.15$. Non-planar waves have the same natural frequency ω_1 and the weakly nonlinear resonance frequency is:

$$\frac{\omega}{\omega_1} = 1 - \tfrac{1}{2}(A + B)\frac{\overline{\eta^2}}{\ell^2}, \tag{16}$$

where $A + B$ is always negative and $A + B = -0.42$ when $h/R \gg 1$. The swirling waves have, therefore, a positive nonlinearity at all fluid depths. This behaviour is confirmed by the fully nonlinear multimodal theory of Faltinsen *et al.* (2003) applied to a square-base container.

2.3. *Multimodal theory*

The small-dimensional modal models using only the generalized coordinate $\eta_n(t)$ and five modes, as discussed above, do not allow calculating hydrodynamic forces on the tank wall nor fluid–structure interactions or take into account more complex forcing where transient effects are of importance. The multidimensional model system, as developed by Faltinsen *et al.* (2000) and others, is capable of treating such complex sloshing and includes intermediate fluid depths where secondary modes become more important. The limitations of the model are that the tank walls must be smooth, vertical and cylindrical. Overturning waves are excluded. The multimodal model is based on a generalized Fourier series representation of the surface elevation in the form of (7) and of the velocity potential, namely

$$\eta(x, y, t) = \eta_n(t)\psi_n(x, y), \quad \phi(x, y, z, t) = R_i(t)\varphi_i(x, y, z), \tag{17}$$

where repeated indices represent summation as above. $\psi_n(x, y)$ are a complete set of orthogonal functions and $\varphi_i(x, y, z)$ a family of harmonic functions. The generalized coordinates $\eta_n(t)$ and $R_i(t)$ are determined by the modal system (coupled system of nonlinear ODE) derived from the free-boundary problem using a variational technique. Faltinsen *et al.* (2003, 2005) treated sloshing in a square-base container retaining nine modal functions.

https://doi.org/10.1017/S0022112007004764 Published online by Cambridge University Press

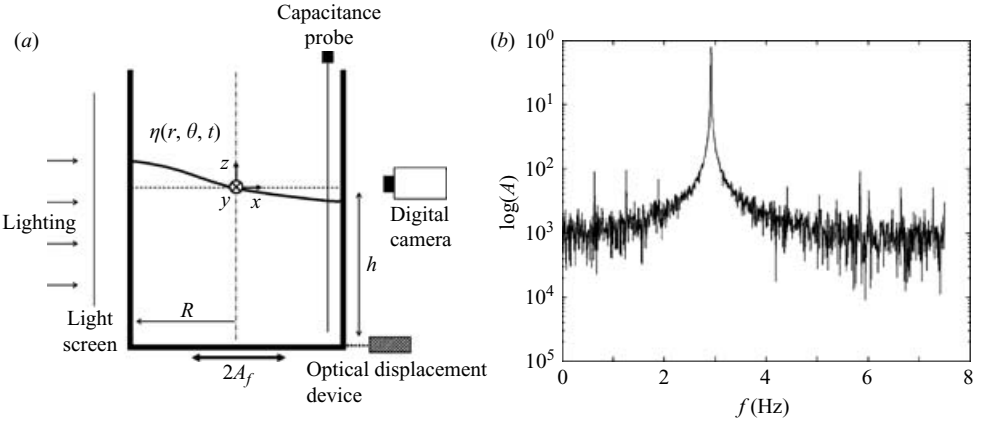


FIGURE 1. (*a*) Experimental set-up. (*b*) Fourier analysis of the excitation signal for $A_f/R = 0.023$.

3. Experimental set-up

The sloshing experiments were conducted in circular cylindrical containers, one of diameter $d = 2R = 300 \pm 4$ mm and 60 cm deep, made of Plexiglas and the other of diameter $d = 156 \pm 0.6$ mm and 25 cm deep, made of Pyrex. The natural periods of the lowest asymmetric modes are, respectively, $T_1 = 2\pi/\omega_1 = 572$ ms and 413 ms. Complementary experiments on wave breaking were conducted in a square-base glass container of base $L = 280 \pm 0.5$ mm and 50 cm in depth of natural period $T_1 = 599$ ms. These containers, filled with water or alcohol to the desired depth h, were mounted on an oscillating table. In the present experiments, the fill ratio was always $h/R > 1.2$ (generally 1.5) satisfying deep-water conditions ($\tanh(k_1 h) > 0.976$ in the dispersion relation). The water used was tap water; distilled water was also used and no difference in the sloshing behaviour was noticed. Alcohol has a kinematic viscosity $\nu = 0.0148\,\mathrm{cm^2\,s^{-1}}$ at 20 °C and a surface tension $\sigma = 22.3\,\mathrm{dyn\,cm^{-1}}$ and this also had no effect on the wave motion (the Bond number $Bo = \rho g R^2/\sigma > 800$). Only the sizes of drops and bubbles produced by breaking are smaller.

The oscillating table is driven by a linear motor with electro-magnetic control (Rexroth INDRAMAT), equipped with an optical precision displacement ruler (Heidenhain). The range of the excitation parameters used was $0.5 \leqslant f \leqslant 5$ Hz and $0.05 \leqslant A_f \leqslant 5$ mm. The frequency and amplitude were measured with an optical displacement probe. The error in frequency is less than 0.005 Hz with fluctuations lower than 0.002 Hz (error < 0.3 % of nominal frequency). In each experiment, the signal of the optical displacement meter was sampled at a frequency of 30 Hz and this increased the error in frequency to < 1 %. The fluctuations in excitation amplitude were less than 3 % in the frequency range of the present experiments. Figure 1(*a*) shows a schematic representation of the experimental configuration with the forcing power spectrum given in figure 1(*b*).

The wave amplitude was measured with capacitance probes that were calibrated before and after each experiment and have a resolution of 0.2 mm. These probes were positioned at about 1/8 of the radius from the tank wall (4 mm for the reservoir of radius $R = 78$ mm and 13 mm for the reservoir of radius $R = 150$ mm) and along a line parallel to the tank movement ($\theta = 0°$, position $P1$) and perpendicular ($\theta = 90°$, position $P2$) to the direction of the tank movement. The probe at $P2$ indicated

https://doi.org/10.1017/S0022112007004764 Published online by Cambridge University Press

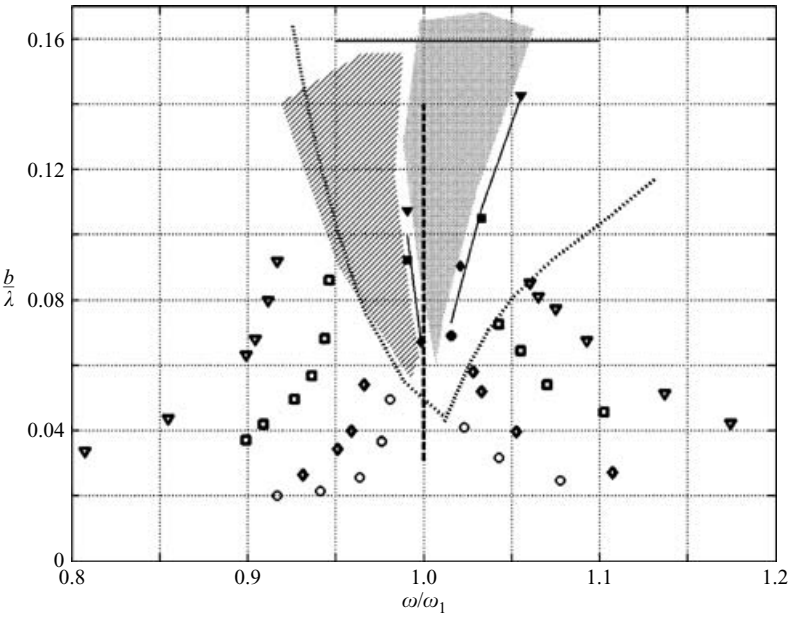


FIGURE 2. Amplitude–frequency diagram for four different forcing amplitudes A_f/R: ▽, planar wave mode 1; ▼, swirling wave mode for $A_f/R = 0.0266$; □, ■, $A_f/R = 0.0133$; ◇, ◆, $A_f/R = 0.0066$; ○, ●, $A_f/R = 0.0033$. A stable swirling wave (dotted region) exists between the filled symbols and chaos to the left of it (hatched region). The dotted branches are the bounds of swirl of Abramson *et al.* (1966). The upper horizontal line indicates $b\omega^2 = g$, giving $b/\lambda = 0.16$ ($\lambda = 3.411R$). The container, filled with water to $h/R \approx 1.5$, has a radius $R = 78$ mm.

whether or not a swirling wave component was present. The shape of the liquid surface was obtained by visualizations using backlighting and image analysis.

4. Frequency domain of steady-state regimes

4.1. *Amplitude response curves*

Figure 2 shows the wave amplitude response $b = \eta(R, \theta, nT)$, at $\theta = 0°$ ($P1$) and $\theta = 90°$ ($P2$) made dimensionless by the wavelength λ, as a function of dimensionless frequency ω/ω_1 for four forcing amplitudes A_f/R. All experimental points correspond to steady-state wave motions. The open symbols indicate planar waves and the closed symbols swirling waves. The wave amplitude is here scaled by the wavelength, $\lambda \equiv \lambda_1 = 3.411R$, because this allows a comparison with the wave-amplitude response curve of a square-base container for instance and gives the wave steepness directly. The amplitude response curves show clearly that the limits of existence of steady-state planar waves depend on both the forcing frequency and amplitude related by the frequency-offset parameter $\beta = (\omega^2 - \omega_1^2)/\varepsilon^2\omega_1^2$. The corresponding frequency domain of existence of the swirling wave mode and of chaos increases with forcing amplitude as expressed by β. For the four dimensionless forcing amplitudes $A_f/R = 0.0266, 0.0133, 0.0066$ and 0.0033 shown in figure 2, the parameter ε (12) is, respectively, $\varepsilon = 0.356, 0.282, 0.224$ and 0.177. The damping ratio for the lowest asymmetric mode of wavenumber $k_1R = 1.841$ is given by (6) in the form $\delta = C_1(\nu^2/R^3g)^{1/4}$ with $C_1 \approx 1$. Using this value of δ, the damping parameter is $\alpha = 2\delta/\varepsilon^2 \approx 0.061, 0.098, 0.155$ and 0.248, respectively, for the four forcing amplitudes and water (for alcohol, the α values are about 20 % larger). These values of the

https://doi.org/10.1017/S0022112007004764 Published online by Cambridge University Press

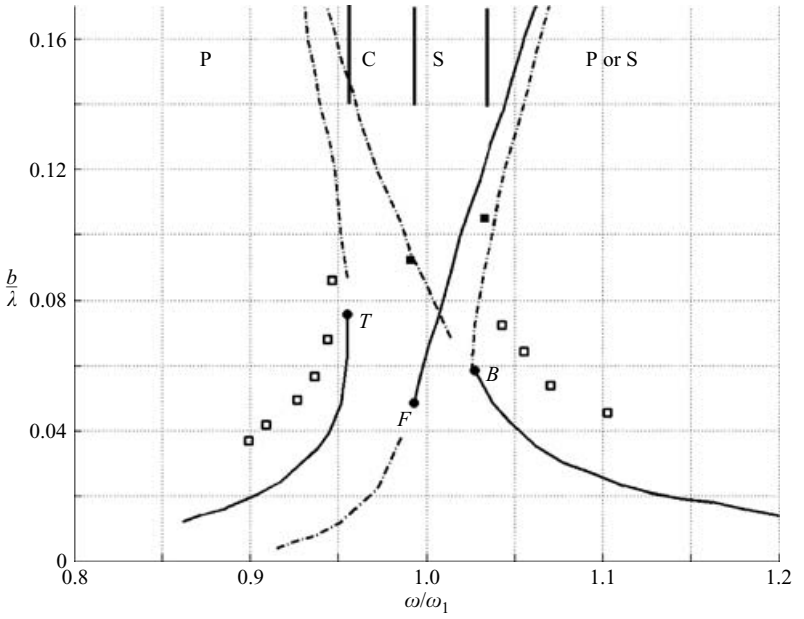


FIGURE 3. Comparisons of the experimental amplitude response of planar waves and swirl wave in a cylindrical container and the response curves determined by the multimodal analysis of Faltinsen *et al.* (2003) for a square-base container of base L, and $A_f/L = 0.008$ ($A_f/\lambda = 0.004$). In the experiments, the excitation amplitude is $A_f/R = 0.0133$ ($A_f/\lambda = 0.0039$). □, experimental planar wave mode; ■, experimental swirling mode determined by increasing (starting from $\omega/\omega_1 < 1$) and decreasing the excitation frequency (starting from $\omega/\omega_1 > 1$). —, stable and —·—, unstable branches of Faltinsen *et al.* (2003). P = plane waves, S = swirl, C = Chaos. B, F and T are the bifurcation points.

damping parameters are indicative of small damping where the resonance curves are qualitatively similar, exhibiting at least four bifurcation points.

Above the natural frequency, $\omega/\omega_1 > 1$, when for a given forcing amplitude the forcing frequency is slowly decreased by small decrements, the planar wave amplitude increases (soft spring behaviour) until a critical frequency is reached at which the motion bifurcates to a swirling wave; this bifurcation point is denoted as β_4 by Miles (1984*b*) and corresponds to point B in figure 3 for a square-base container. The same bifurcation to a swirling wave mode is obtained when the forcing frequency is fixed and the forcing amplitude is increased by a small increment. The stability boundary is, therefore, well defined. This stability boundary agrees with that obtained by Abramson *et al.* (1966), indicated in figure 2 by the right-hand branch of the dotted line. However, Abramson *et al.* do not give the stable swirl wave curve and indicate a swirl wave where chaos exists. At a frequency near to $\omega/\omega_1 = 1$, the swirl wave mode bifurcates to chaos via a limit cycle and period doubling (Funakoshi & Inoue 1988) at the Hopf bifurcation point denoted β_2 by Miles (1984*b*) (corresponding to point F in figure 3). The accuracy of the results as presented in figure 2 is about 1 % in ω/ω_1, which is insufficient for analysing this Hopf bifurcation. It would have required special focus on this point, but this was not the purpose of the present experiments.

When starting at $\omega/\omega_1 < 1$ and then increasing the forcing frequency by small increments, the planar wave amplitude for a given forcing amplitude increases with frequency until the wave amplitude reaches a turning point (point β_3 corresponding

https://doi.org/10.1017/S0022112007004764 Published online by Cambridge University Press

to point T in figure 3) and grows rapidly until wave breaking occurs. This regime is referred to as chaos (Miles 1984*b*; Faltinsen *et al.* 2003, see figure 3). The chaos regime overlaps with what was classified as swirl by Abramson *at al.* (1966). The upper horizontal line in figure 2 is the limit where the wave amplitude is such that the downward acceleration $b\omega^2$ is equal to gravity. As will be discussed in § 5, breaking requires that the downward acceleration be equal to or larger than gravity (Taylor 1953). However, chaotic sloshing can occur without breaking, that is, without reaching amplitudes such that the downward wave crest acceleration is equal to gravity.

Although the geometry is different, it is of interest to compare the present results obtained in a circular cylindrical container with the solutions of the modal equations for a square-base container presented in Faltinsen *et al.* (2003). One forcing amplitude, namely $A_f/R = 0.0133$ is close to their forcing amplitude $A_f/L = 0.008$, where L is the base dimension. When made dimensionless by the primary mode wavelengths λ ($\lambda = 3.411R$ and $\lambda = 2L$, respectively) the dimensionless forcing amplitudes are close. Figure 3 shows that there is qualitative agreement between the experimental results obtained in a circular cylinder and the modal results obtained for a square-base container (the square-like wave branch which exists in a square-base container is not shown). It would have been desirable to compare the experimental results with the modal model solutions of Gavrilyuk *et al.* (2000) who obtained the response curves associated with the lowest modes for a circular cylinder. Effects of higher modes were not accounted for, so that the results are not really representative of experiments. Contributions of higher modes to swirling are considerable and many details on that are elaborated by Faltinsen *et al.* (2006).

A better representation of the bounds of steady-state wave motion is to plot the dimensionless forcing amplitude A_f/R as a function of ω/ω_1. This is shown in figure 4, the symbols are the same as in figure 2. The relation between A_f/R and ω/ω_1 is given by the frequency-offset parameter β and the bounds are given by the specific values of β_2, β_3, β_4, β_5 or β_6 determined by Miles (1984*b*). For $\alpha^2 \ll 1$, the bifurcation point β_1 does not exist and $\beta_2 = -0.36$. The other bifurcation points are to leading order (higher-order terms are in α^2 and amount to less than 2 % of the leading-order terms) $\beta_3 = -1.55$, $\beta_4 = 0.735$, $\beta_5 = 0.108/\alpha^2$ ($\beta_6 = 0.717$). In figure 4, the lines corresponding to these bifurcation points are indicated. These lines are given by:

$$\frac{A_f}{R} = \frac{1}{1.684}\left[\frac{(\omega/\omega_1)^2 - 1}{\beta_i}\right]^{3/2}, \tag{18}$$

where $i = 2, 3, 4, 5, 6$.

4.2. *Steady-state planar waves*

The amplitude of steady-state planar waves, made dimensionless by the forcing amplitude A_f, is plotted in figure 5. The large dispersion in measured wave amplitudes is partly due to the relatively small values of wave amplitudes, particularly when the forcing amplitude is small and the frequency offset parameter is large. The error in wave amplitude, measured with the capacitance probes, is generally ± 0.2 mm. The time after initiation of the forcing when the steady-state amplitude is determined, introduces a further error. Theoretically, t/T must go to infinity, but, in practice, the measurement is validated when $t/T = 100$. Furthermore, secondary modes become increasingly important when the wave amplitude is small and this introduce fluctuations. Fourier analysis of the signal showed that the energy in the secondary modes of frequency $2\omega_1$ is of the same order as the energy of the dominant mode when the wave amplitude $b < 8$ mm. At larger wave amplitudes, the energy of the primary mode is an order of magnitude larger.

https://doi.org/10.1017/S0022112007004764 Published online by Cambridge University Press

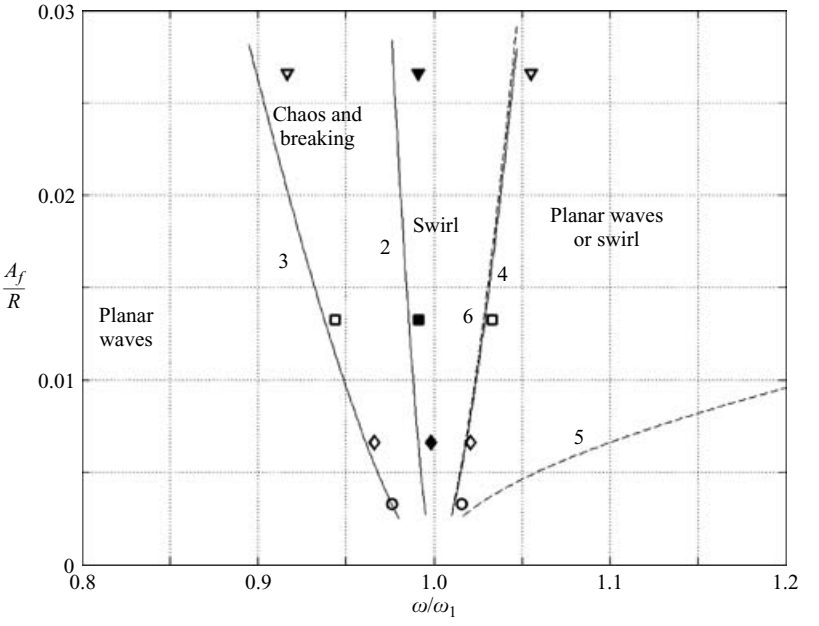


FIGURE 4. Phase diagram of dimensionless forcing amplitude A_f/R versus frequency ratio ω/ω_1 for four forcing amplitudes (see figure 2 for symbols). The solid lines are the bounds where the number of fixed points changes, given by $\omega/\omega_1 = (\beta_i \varepsilon^2 + 1)^{1/2}$, $i = 2, 3, 4$. The bounds corresponding to the bifurcation points β_5 and β_6 are indicated by dashed lines.

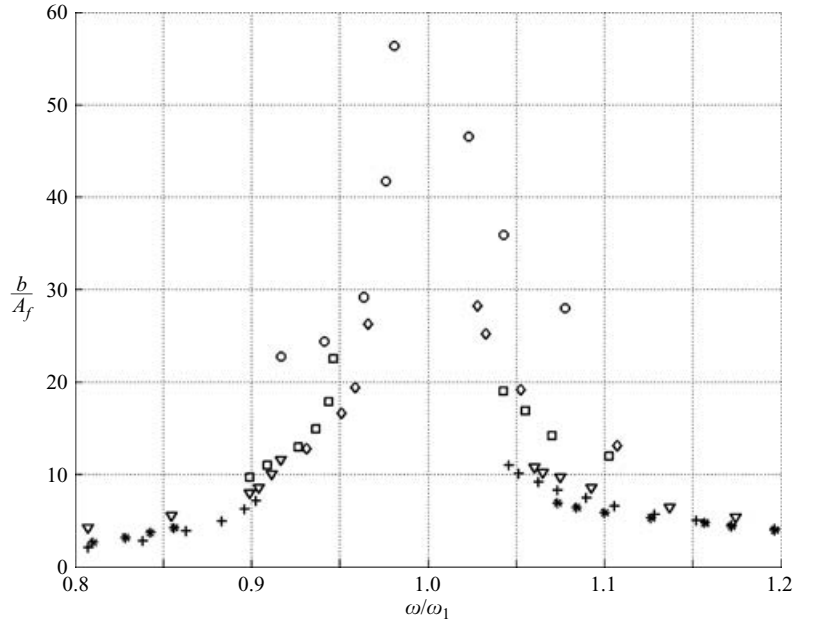


FIGURE 5. Amplitude response of planar waves for different forcing amplitudes. Symbols are the same as in figure 2. The points *, $A_f/R = 0.045$ and +, $A_f/R = 0.023$ are from Abramson *et al.* (1966). The wave amplitude b is here scaled by A_f.

https://doi.org/10.1017/S0022112007004764 Published online by Cambridge University Press

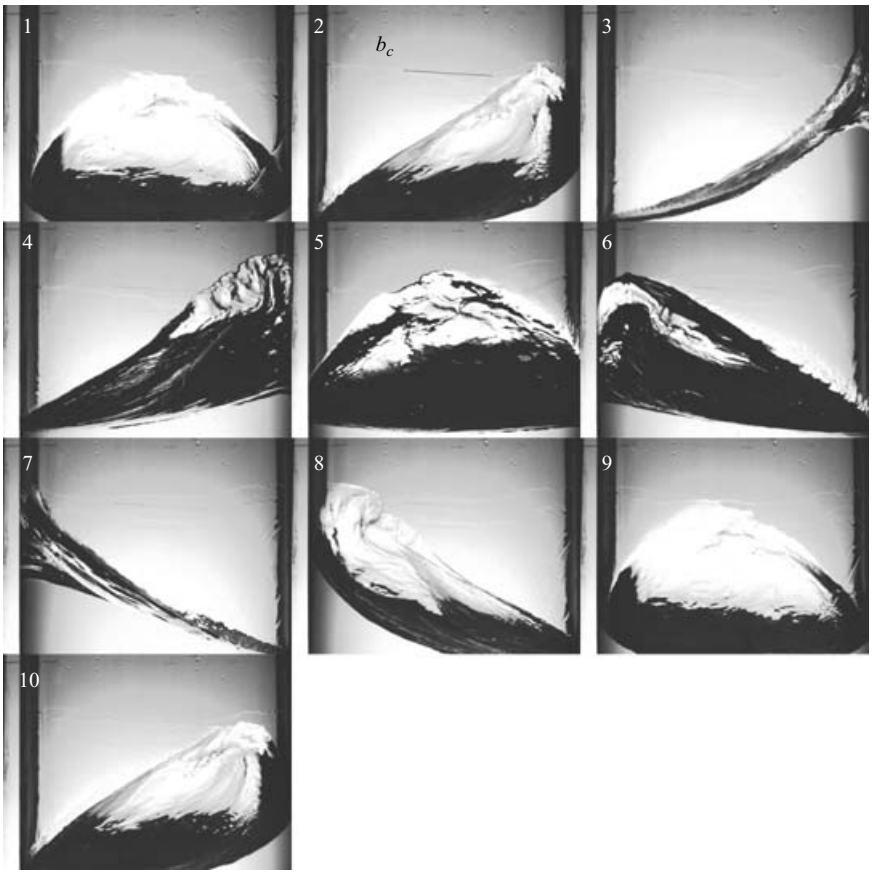


FIGURE 6. Images of a swirling wave in circular cylinder of radius $R = 150$ mm partially filled with water. Views are in the direction normal to the tank motion. The time between two images is 67 ms. The ten images represent slightly more than one wave period $T = 2\pi/\omega = 570$ ms. $h/R \approx 1.2$, $\omega/\omega_1 \approx 1.02$, $A_f/R = 0.023$.

Linear oscillators would suggest that $b/A_f = C_1(K^2/|1 - K^2|)$ where $K = \omega/\omega_1$. Although for $\omega/\omega_1 < 1$ the data would collapse reasonably well by this scaling, this is not the case for $\omega/\omega_1 > 1$. The weakly nonlinear theory of Miles (1984*b*) predicts the asymmetry shown in figure 5. The planar wave-amplitude response curves terminate at the fixed points $\beta_3 = -1.55$, and $\beta_4 = 0.735$, giving, respectively, $\omega/\omega_1 = (-1.55\varepsilon^2 + 1)^{1/2}$ and $\omega/\omega_1 = (0.735\varepsilon^2 + 1)^{1/2}$. For the smallest excitation amplitude $A_f/R = 0.0033$, the corresponding values ω/ω_1 are 0.976 and 1.011.

4.3. *Robustness of the swirling wave*

The swirling wave motion, also referred to as rotary sloshing by Ibrahim (2005), is very robust. Figure 6 shows images of a large-amplitude ($b > 0.16\lambda$) swirling wave taken at 67 ms intervals which corresponds to 0.12 wave periods. There are fairly large disturbances in the vicinity of the (flat-top) wave crest (local breaking), but the wave remains stable. Nonlinear waves can transfer angular momentum to the whole liquid column that starts to rotate (Faller 2001). The result is a Doppler shift, causing the wave frequency to increase with respect to the forcing frequency. This Doppler shift is clearly demonstrated by figure 7(*a*), where the swirl wave amplitude is plotted as a

https://doi.org/10.1017/S0022112007004764 Published online by Cambridge University Press

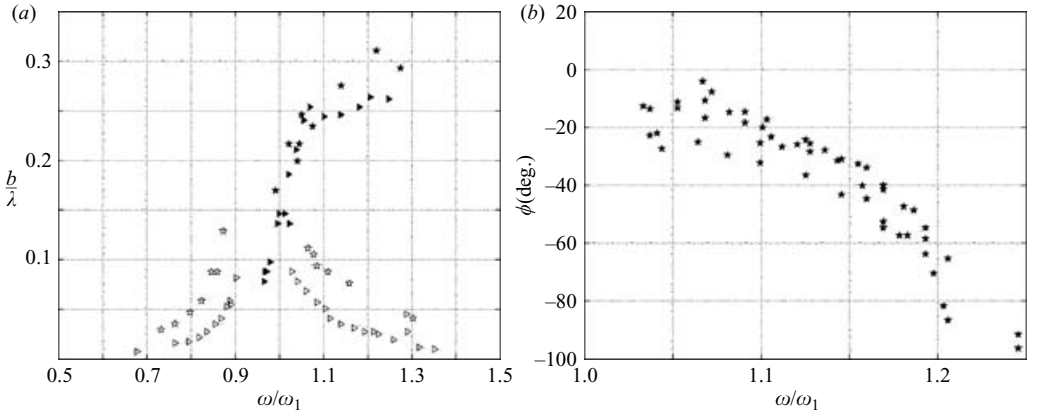


FIGURE 7. (*a*) Dependency of wave amplitude on forcing frequency. The tank radius is $R = 150$ mm filled with water to $h/R \approx 1.5$. ▷, plane wave; ►, swirling wave for $A_f/R = 0.023$; ☆, ✶, $A_f/R = 0.045$; (*b*) variation of phase lag of the swirling wave.

function of forcing frequency. Once the swirl is established, it can be maintained up to fairly large forcing frequencies, here up to $\omega/\omega_1 \approx 1.3$, when the forcing frequency is increased by small increments. This value is larger than that observed by Faller (1983). When the forcing frequency is further increased by a small amount, the swirl wave suddenly collapses and the motion switches to a small-amplitude out-of-phase planar wave motion. In the weakly nonlinear theory, the non-planar resonance curve terminates at the fixed points $\beta_2 = -0.36$, and $\beta_5 = 0.108/\alpha^2$ (or β_6). For $A_f/R = 0.023$ and a dissipation coefficient $\alpha \approx 0.06$, the fixed point β_5 is at $\omega/\omega_1 \approx 2$ and β_6 at $\omega/\omega_1 \approx 1.045$, which do not agree with the experimental value. The Hopf bifurcation point β_2 is at $\omega/\omega_1 = 0.979$. This would correspond to the experimental value, but the precise behaviour at β_2 is not resolved in the present experiments because we did not give special attention to this point. Funakoshi & Inoue (1988) investigated this bifurcation point in great detail.

The swirling wave is initially nearly in phase with the forcing and as the forcing frequency is increased the phase lag increases up to a maximum of $-\pi/2$ (figure 7*b*). This phase lag was determined by correlating the output of the optical probe, measuring the container displacement, with the signal of the capacitance probe located at $P1$. Ibrahim (2005) mentions a phase angle of 90° for the swirling wave, referring to Abramson *et al.* (1966). However, this phase lag is only observed just before the collapse of the swirling mode. Figure 7(*a*) indicates two distinct dependencies of the swirl wave amplitude on forcing frequency for fixed forcing amplitude. In the range of $1 < \omega/\omega_1 \leqslant 1.08$, the wave amplitude increases nearly linearly with forcing frequency as predicted by the multimodal theory (see figure 3). For $\omega/\omega_1 > 1.08$ and up to collapse, the wave amplitude exhibits only a small increase from $b/\lambda \approx 0.26$ to about 0.30. There is continuous local wave breaking near the wave crest, but as long as the forcing frequency, remains below the collapse frequency, the swirl wave is maintained. In the experiment corresponding to figure 7, the wave speed near the container boundary before collapse is $V_\theta = \omega R = 212\,\mathrm{cm\,s^{-1}}$, indicating a Doppler shift consistent with a fluid velocity of about 10 % of V_θ. Faller (2001) measured the fluid rotation generated by a large-amplitude swirling wave motion forced by a rotary oscillation (rotillation) of the container and reports a fluid azimuthal velocity of up to 25 % of the wave speed. The dimensionless amplitude of the wave in his experiments

https://doi.org/10.1017/S0022112007004764 Published online by Cambridge University Press

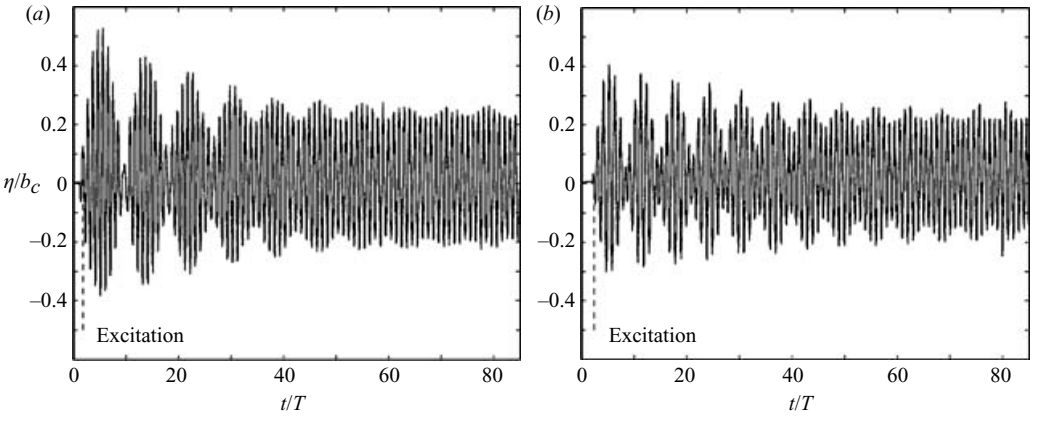


FIGURE 8. Non-dimensional wave amplitude, η/b_c, versus time, t/T, for (*a*) $\omega = 0.86\omega_{11}$; (*b*) $\omega = 1.17\omega_1$. $T_1 = 2\pi/\omega_1 = 413$, $T = T_1/K$ and $b_c = 1.841/R$. The liquid is water, $\nu = 0.01\,\mathrm{cm^2\,s^{-1}}$, $R = 78\,\mathrm{mm}$ and $h/R \approx 1.5$. $K = \omega/\omega_1$.

is of the same order as in the present experiments. Faller mentions that wave breaking (spilling at wave crest) produces a turbulent wave motion and this favours the transfer of wave angular momentum to the fluid angular momentum, as was proposed by Prandtl (1949). The larger fluid azimuthal velocity in Faller's experiments may be due to the rotary forcing that imposes a swirling wave at all amplitudes.

5. Transient regimes

5.1. *Transition to steady-state planar mode*

When starting to force the container at a frequency $\omega = K\omega_1$ with $K \neq 1$, the wave motion behaves like a damped oscillator with the superposition of two frequencies, namely ω and ω_1. Figures 8(*a*) and 8(*b*) show the wave amplitudes as a function of time for $K = 0.86$ and $K = 1.17$, respectively, measured near the container wall at $\theta = 0^\circ$ (position $P1$). The dimensionless forcing amplitude is $A_f/R = 0.045$. As expected, a strong beating is observed at a frequency $|\omega_1 - \omega|$. Fourier analysis of the signal (not shown here) at regular time intervals exhibits the time evolution of the energy contained in the three different frequencies, namely the forcing and natural frequencies and the difference between the two. The Fourier analysis further shows that the second resonance mode of frequency ω_{12} is also present, but its energy is negligibly small. Because of the relatively large forcing amplitude, higher harmonics are practically absent. As expected, the amplitude of the natural frequency oscillation decays exponentially and is negligible after about 100 periods. The measured damping rate κ is close to $0.06\,\mathrm{rad\,s^{-1}}$. For $R = 78\,\mathrm{mm}$ the frequency is $\omega_1 = 15.2\,\mathrm{rad\,s^{-1}}$, giving $\delta = \kappa/\omega_1 = 0.0039$. Thus, the coefficient $C_1 \approx 1$ in $\delta = C_1 \nu^{1/2} R^{-3/4} g^{-1/4}$.

Royon-Lebeaud (2005) also determined the damping rate by stopping the forcing after the steady-state planar wave was established and measured the wave amplitude as a function of time. The measurements were stopped when the amplitude fell below 0.2 cm. The constant C_1 in (6) was generally larger than 1 ($C_1 \approx 1.3$) with a fairly large scatter. When the forcing is stopped, the steady-state wave amplitude jumps within two to three periods to a larger or lower value depending on whether the forcing frequency is, respectively, larger or lower than the natural frequency. The wave frequency of the planar waves switches to the natural frequency conserving

https://doi.org/10.1017/S0022112007004764 Published online by Cambridge University Press

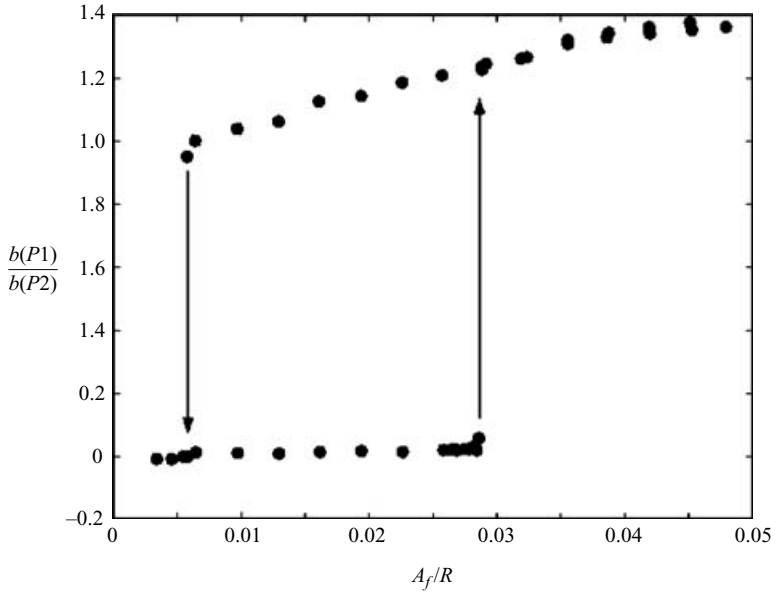


FIGURE 9. Bifurcation diagram from planar wave motion to swirling and swirl/planar wave by increasing the forcing amplitude A_f/R and then decreasing it, keeping the forcing frequency constant at $\omega/\omega_1 = 1.07$; $h/R = 1.6$, $R = 78$ mm.

the ratio of kinetic to potential energy in the form $(b\omega)^2/gb = (b_1\omega_1)^2/gb_1$, giving $b_1 = b(\omega/\omega_1)^2$, where b_1 is the wave amplitude at ω_1.

5.2. *Transition from steady-state planar waves to swirl*

When starting at $\omega > \omega_1$ and then approaching resonance by decreasing the forcing frequency in small steps, the out-of-phase planar wave bifurcates to a swirling mode that is practically in phase with the container motion. Here we consider the transition from planar wave motion to a swirl wave at fixed forcing frequency by increasing the forcing amplitude. The bifurcation diagram is shown in figure 9 where the ratio of the amplitudes of swirl wave to planar wave is plotted as a function of forcing amplitude. Initially, at small values of A_f/R, the movement is a planar wave mode. When A_f/R reaches a critical value, which depends on forcing frequency, here fixed, a bifurcation to a swirling mode takes place; its amplitude increases exponentially (figure 10). This bifurcation corresponds to β_4 in Miles' (1984*b*) notation. For $\alpha \ll 1$, $\beta_4 = 0.735$, which gives at the bifurcation point $A_f/R = 0.028$ a frequency ratio $\omega/\omega_1 = 1.047$ that is somewhat less than the experimental value 1.07. Figure 9 shows that when the swirl wave is established, in a time of about 60 periods, it is very robust. It persists not only up to large forcing amplitudes which is expected according to figure 2, but also down to fairly small forcing amplitudes which is not obvious. This large hysteresis might be favoured by fluid rotation. However, at the wave amplitudes in question ($b/\lambda \leqslant 0.18$) the fluid rotation is weak. Furthermore, the time interval between each step in forcing amplitude is about 10^3 wave periods which would allow the fluid rotation to spin down; the spin-down time $\tau_s = h/(\nu\Omega)^{1/2}$ is about 200 wave periods. The planar wave mode is recovered when $A_f/R \leqslant 0.006$ and the swirl wave amplitudes at positions $P1$ and $P2$ are equal just before collapse of the swirl; the swirl wave amplitude has decreased from 4.2 cm ($b/R = 0.538$) to 3.2 cm. This bifurcation diagram would indicate a subcritical bifurcation. However, it is not possible to increase the wave

https://doi.org/10.1017/S0022112007004764 Published online by Cambridge University Press

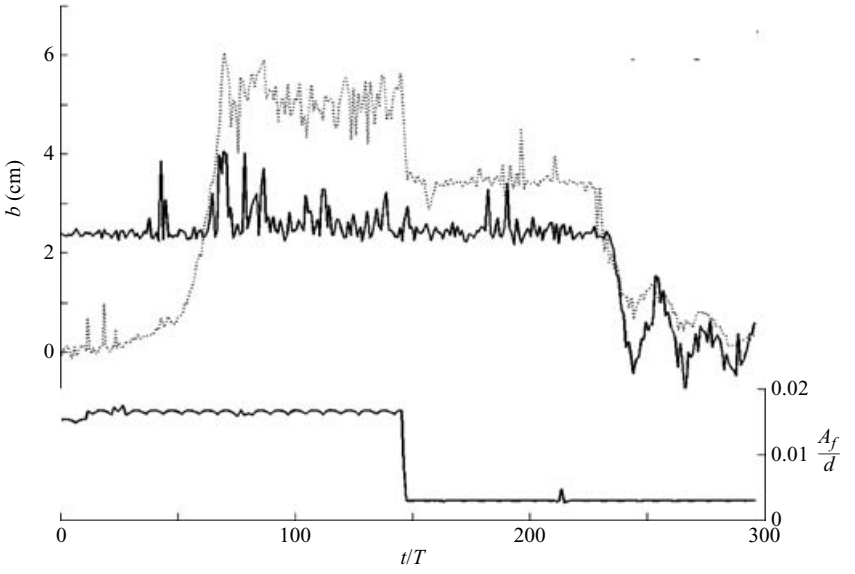


FIGURE 10. Temporal evolution of planar and swirl wave amplitudes. The upper part of the figure represents the amplitudes measured by each probe: —, probe at $P2$; ..., probe at $P1$. The lower part shows the imposed variation in forcing amplitude, right-hand scale $A_f/2R$. Cylindrical container $R = 78$ mm filled with water to $h/R = 1.5, \omega/\omega_1 = 1.07$. $T = 2\pi/\omega = 385$ ms.

amplitude sufficiently for the bifurcation to a swirl wave to take place at a forcing amplitude below the critical value β_4.

Figure 10 shows the temporal evolution of the wave amplitudes measured at $P1$ and $P2$. When the forcing amplitude is just below the critical amplitude (here made dimensionless by $d = 2R$) which is $A_f/2R = 0.014$ for $\omega/\omega_1 = 1.07$, the surface displacement measured by the probe located at $P2$ is practically zero; there is only planar wave motion. A slight increase in A_f causes the motion to bifurcate to a swirl wave with an exponential growth in wave amplitude. A step reduction in forcing amplitude to $A_f/2R = 0.0035$ causes the swirl wave amplitude to decay in a time of about 100 to 150 wave periods.

The low-frequency fluctuations in the capacitance probe signal shown in figure 10 are actual fluctuations of the free-surface elevations owing to capillary waves and perhaps harmonics. These can be ± 5 mm during transients. The spikes in the signal are electronic noise. These spikes could have been eliminated by low-pass filtering, but this was not done because it does not alter the results.

6. Chaotic sloshing and wave breaking

6.1. *Chaotic sloshing and breaking conditions*

Chaotic sloshing occurs between bounds 2 and 3 indicated in figure 4. The frequency range where chaotic sloshing takes place depends on the forcing amplitude, expressed by the frequency-offset parameter β. When the experiments are started at forcing frequencies below resonance and steady-state planar wave motion is established, a small increase in forcing frequency leads to a rapid increase in wave amplitude if the turning point is crossed. Rapid increase in wave amplitude and wave breaking occurs in a similar way in the whole range $\beta_3 < \beta < \beta_2$ except near β_2 where chaos is

https://doi.org/10.1017/S0022112007004764 Published online by Cambridge University Press

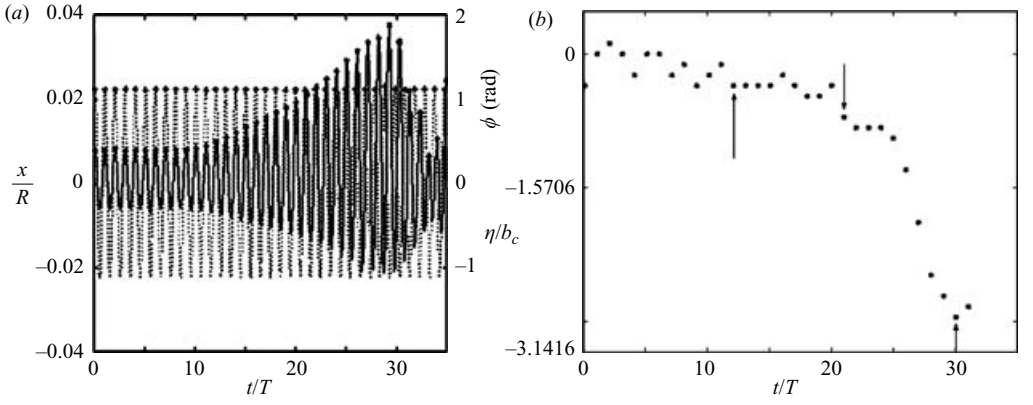


FIGURE 11. (*a*) Time evolution of dimensionless wave amplitude b/b_c versus dimensionless time. (*b*) Corresponding phase lag ϕ (rad). The forcing amplitude (left-hand scale in *a*) is $A_f/R = 0.022$, $R = 150$ mm, $h/R = 1.5$. Up to $t/T = 10$, the forcing amplitude was $\omega/\omega_1 = 0.89$, then it was increased to $\omega/\omega_1 = 0.92$. $T = 2\pi/\omega = 622$ and 640 ms, $b_c = 0.54R$.

possible without breaking. The growth in wave amplitude near β_3 and wave breaking is illustrated in figure 11(*a*) where the surface displacement as a function of time, measured with the capacitance probe located 1.3 cm ($0.08R$) from the container wall at point $P1$, is shown. The surface displacement is made dimensionless by b_c and time by the forcing period $T = 2\pi/\omega$ (calculated with $\omega = 0.89\omega_1$). The scale on the left-hand side is the container displacement x/R. Up to $t/T = 10$ (the experiments were of course started well before so that the free oscillations had time to decay), the forcing frequency was kept constant at $\omega/\omega_1 = 0.89$ and the motion is seen to consist of steady-state planar waves in phase with the container motion. Then the forcing frequency was increased to $\omega/\omega_1 = 0.92$ leading to a growth in wave amplitude. The dimensionless frequency corresponding to the fixed point $\beta_3 = -1.52$ is $\omega/\omega_1 = 0.911$. It is seen in figure 11(*a*) that as the wave amplitude grows, the motion becomes more and more asymmetric with the positive maximum surface displacements reaching nearly twice the negative displacements. The motion is initially in phase with the forcing, but then the phase lag increases with wave amplitude (figure 11*b*). When $b > b_c$, the phase lag increases rapidly to $-\pi/2$ and is $-\pi$ at collapse. After breaking of the planar wave, an irregular swirl is generated and when the irregular sloshing motion has sufficiently decayed, the planar wave grows again in amplitude until breaking. This behaviour occurs quasi-periodically.

Figure 12(*a*) shows the dimensionless surface elevation at $P1$, $\eta(R, 0, t)/b_c$ versus dimensionless time for $\omega/\omega_1 = 0.98$, that is close to β_2, and $A_f/R = 0.0033$. Initially, the sloshing consists of planar wave motion of temporal growth in wave amplitude. Near maximum wave amplitude, here $b \approx 0.6b_c$, the surface elevation at $P2$ starts to grow rapidly and the amplitude at $P1$ decreases. The following motion is chaotic with irregularly varying surface displacements at $P1$ and $P2$ indicating irregular non-planar motion. This is chaos without actual wave breaking ($b\omega^2 < g$). At time marked t_1, the motion is again regular with a temporal growth of the planar wave amplitude up to t_2 where the amplitude at $P2$ starts to grow again; the amplitude at $P2$ is maximum at t_3 and the amplitude at $P1$ is at a minimum. This is indicative of irregular non-planar wave motion. The growth and collapse of the planar wave motion is seen to be quasi-periodic, of period $(t_4 - t_1) \approx 120T$.

https://doi.org/10.1017/S0022112007004764 Published online by Cambridge University Press

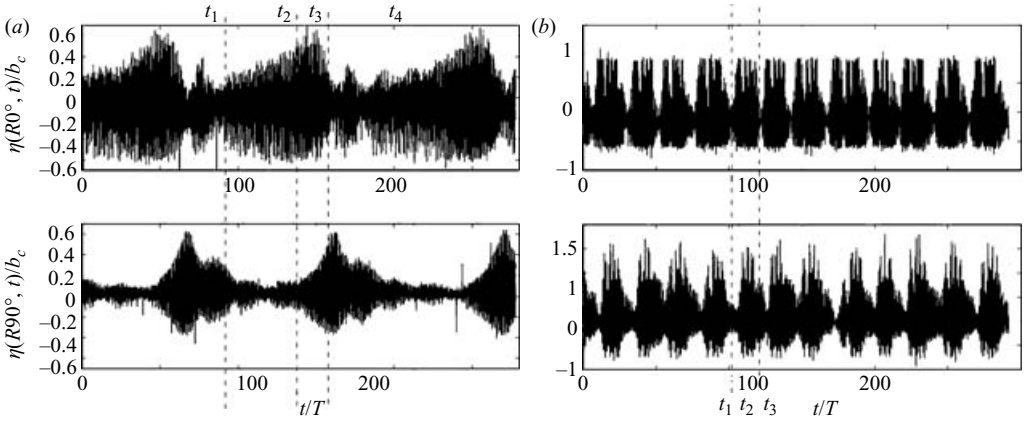


FIGURE 12. Time evolution of wave amplitudes at P_1 ($\theta = 0°$) and P_2 ($\theta = 90°$) in circular container of $R = 78$ mm filled with water to $h/R \approx 1.5$, $\omega/\omega_1 = 0.98$, $T = 421$ ms. (*a*) $A_f/R = 0.0033$; (*b*) $A_f/R = 0.021$.

The time evolution of wave amplitude shown in figure 12(*a*) is similar, but different in detail, to that measured by Funakoshi & Inoue (1988) at 0° and 90° for $T_r = (T - T_1)/T_1 = 0.0196$, that corresponds to $\omega/\omega_1 = 0.981$ ($\omega/\omega_1 = 1/(T_r + 1)$), and $A_f/R = 0.0055$. The extreme sensitivity to forcing amplitude at this forcing frequency is apparent when comparing the time evolution measured by Funakoshi & Inoue with that shown in figure 12(*a*) for $A_f/R = 0.0033$. This dependency on A_f/R is clearly seen when for the same forcing frequency the forcing amplitude is increased by a factor of about 7 to $A_f/R = 0.021$ (figure 12*b*). The wave amplitude at breaking is in this case much larger ($b > b_c$) and the quasi-periodicity of the bursts of alternating planar wave motion and swirl decreases substantially to a burst period of about $20T$. Unfortunately, the wave amplitude measured with the probe located at $P1$ (figure 12*b*) saturates at about $b/b_c \approx 1$. This saturation or cutoff occurred because the capacitance probe at $P1$ was too deep in the water. This does not, however, alter the burst frequency; the actual maximum amplitude is close to $b/b_c \approx 1.6$ as measured by the probe located at $P2$. When comparing the signals at $P1$ and $P2$, it can be seen that there is regular swirl when the wave amplitude has reached a maximum. With increasing excitation amplitude, the regularity of the swirl increases, that is to say, when the amplitude at $P2$ grows, its correlation with the amplitude measured at $P1$ increases (taking into account the azimuthal rotation of $\pi/2$ between the two signals).

Figure 13(*a*) shows the burst frequency and figure 13(*b*) the percentage of regular swirl as a function of dimensionless excitation amplitude $A_f/2R$. The burst frequency has been determined from a spectral analysis of the envelope fitted through the wave amplitudes of the capacitance probe signal located at $P2$. The percentage of regular swirl has been obtained from the correlation between the capacitance probes located at $P1$ and $P2$, taking into account the $\pi/2$ azimuthal rotation. For forcing amplitudes $A_f/2R < 0.0015$ there is no regular swirling mode and no burst frequency can be determined. For conditions corresponding to figure 12(*a*) ($A_f/2R = 0.0016$) there is a clear burst frequency, but practically no regular swirl. In the range $0.0015 \leqslant A_f/2R \leqslant 0.013$, the burst frequency increases slowly and the fraction of regular swirling wave mode increases rapidly from 0 to about 80 %. For forcing amplitudes $A_f/2R = 0.025$, a steady swirl wave regime is approached. When

https://doi.org/10.1017/S0022112007004764 Published online by Cambridge University Press

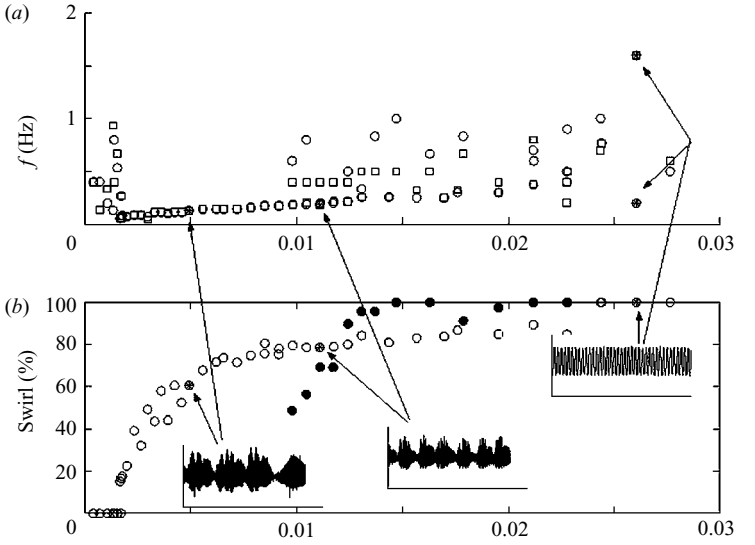


FIGURE 13. (*a*) Burst frequency and (*b*) percentage of regular swirl, versus forcing amplitude A_f/d ($d = 2R$) for $\omega/\omega_1 = 0.98$. $R = 78$ mm. Open symbols, increasing the forcing amplitude; solid symbols, decreasing the forcing amplitude. The signals inserted in (*b*) are signals of the capacitance probe at $P2$.

the forcing amplitude is decreased, regular swirl is maintained down to $A_f/2R > 0.013$ and then there is a more rapid decrease in regular swirl. Note that this behaviour is observed for $\omega/\omega_1 = 0.98$. At this frequency, when the forcing amplitude is increased, the bifurcation point β_2 shifts to smaller values of ω/ω_1 (figures 2 and 4); for $A_f/R = 0.05$, the bifurcation point β_2 is at $\omega/\omega_1 = 0.96$, whereas for $A_f/R = 0.0033$ it is at $\omega/\omega_1 = 0.996$. Therefore, at small forcing amplitudes, the value $\omega/\omega_1 = 0.98$ is in the chaotic regime, and at larger forcing amplitudes, the chaos/swirl bifurcation point is crossed completely. At intermediate forcing amplitudes, the motion switches between chaos and regular swirl in a quasi-periodic manner.

In the chaotic regime, the wave amplitude grows, to first approximation, linearly in time (figure 11) and is nearly proportional to forcing amplitude in the form

$$\frac{b}{R} \approx C_2 \pi \left(\frac{A_f}{R}\right)^n \frac{t}{T}. \tag{19}$$

Linear oscillator theory suggests $n = 1$. Taking this value of n, the constant $C_2 = 0.3$ to 1.5 depending on initial conditions. In general, the growth rate was found to be larger when the wave amplitude in the chaotic regime grows from rest, whereas in the case of an established planar wave motion with a following small forcing frequency increase to the chaotic regime, as shown in figure 11, the growth rate is less. Miles' theory would suggest $n = 2/3$ giving $\mathrm{d}(b/R)/\mathrm{d}\tau = 0.70C_2$, where τ is the slow dimensionless time scale $\tau = (\varepsilon^2 \omega t)/2$. For large wave amplitudes, the weakly nonlinear theory is no longer valid and the exponent may deviate from $n = 2/3$.

Figure 14 shows the complexity of the motion at breaking; images are taken at 60 ms time interval. These images were taken in the container of $R = 150$ mm at $\omega/\omega_1 = 0.98$ and $A_f/R = 0.022$ corresponding closely to conditions of figure 12(*b*). The natural wave period is 580 ms. The motion is viewed in the direction of the container motion. In figure 14(*a*) breaking begins and as the wave crest retreats,

https://doi.org/10.1017/S0022112007004764 Published online by Cambridge University Press

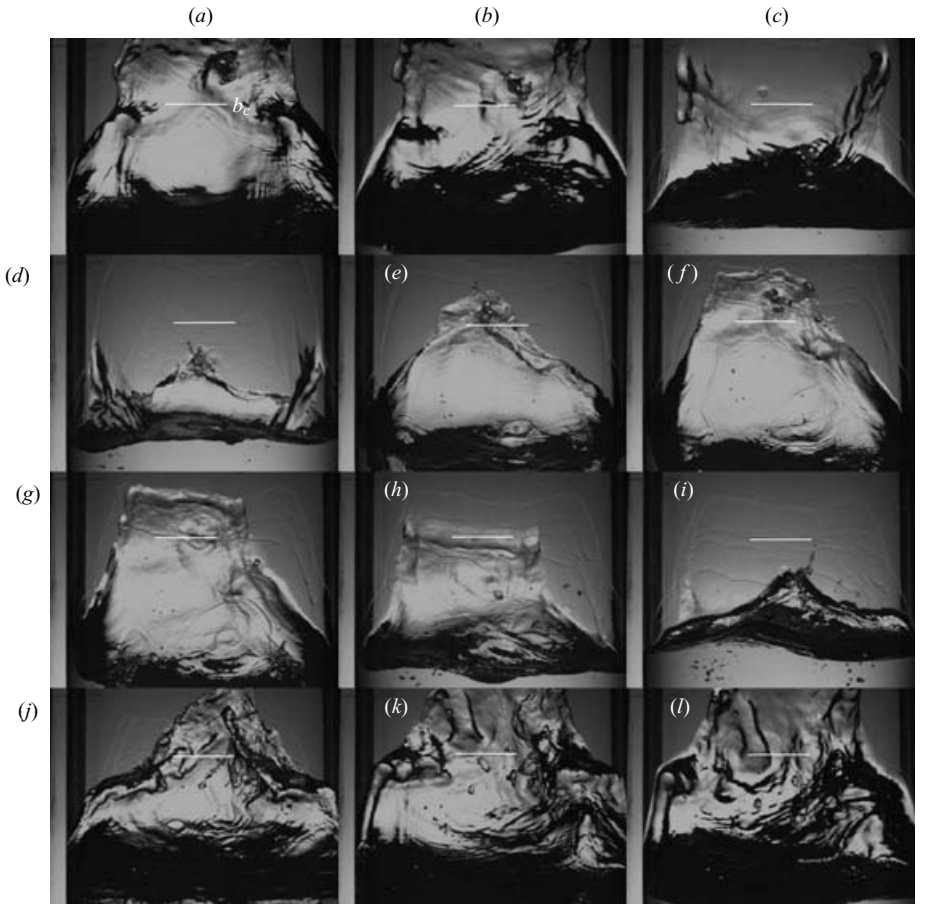


FIGURE 14. Wave breaking viewed in the direction of the container motion in container of $R = 150$ mm for $\omega/\omega_1 = 0.98$ and $A_f/R = 0.023$. The time interval between images is 60 ms and $T = 580$ ms. The sequence of images is from left to right and top to bottom.

ligaments are left behind (figure 14*c*, *d*). The wave crest moving up in figure 14(*e–j*) is on the opposite face (front wall) of the container and has its maximum in figure 14(*f*) that is half a period later. Then, the motion is more and more asymmetric and a swirling wave motion is initiated (figure 14*k*, *l*). An important point to notice is the height of the wave crest that is much larger than b_c. However, the liquid mass that is projected upward to a height $\approx 1.7b_c$ is composed of a layer of approximate thickness $0.1R$. Capillary effects are clearly visible at the edges of this layer (bulge formation) indicating that this liquid mass is under nearly free-fall conditions.

6.2. *Breaking scenarios*

In the whole chaotic regime, wave breaking and collapse is similar to the images shown in figure 14 except that further away from the swirl wave boundary there is less or no regular swirl generated when the planar wave motion collapses. In figure 14(*a–c*), it can be seen that the wave crest is crosswise destabilized with wavelength equal to the layer width (equal to about R). The crest has two maxima at the edges of the layer and then, a period later (figure 14*k*, *l*), the pattern is repeated, but is less regular. Therefore, the frequency of this cross-wave can be considered to be equal

https://doi.org/10.1017/S0022112007004764 Published online by Cambridge University Press

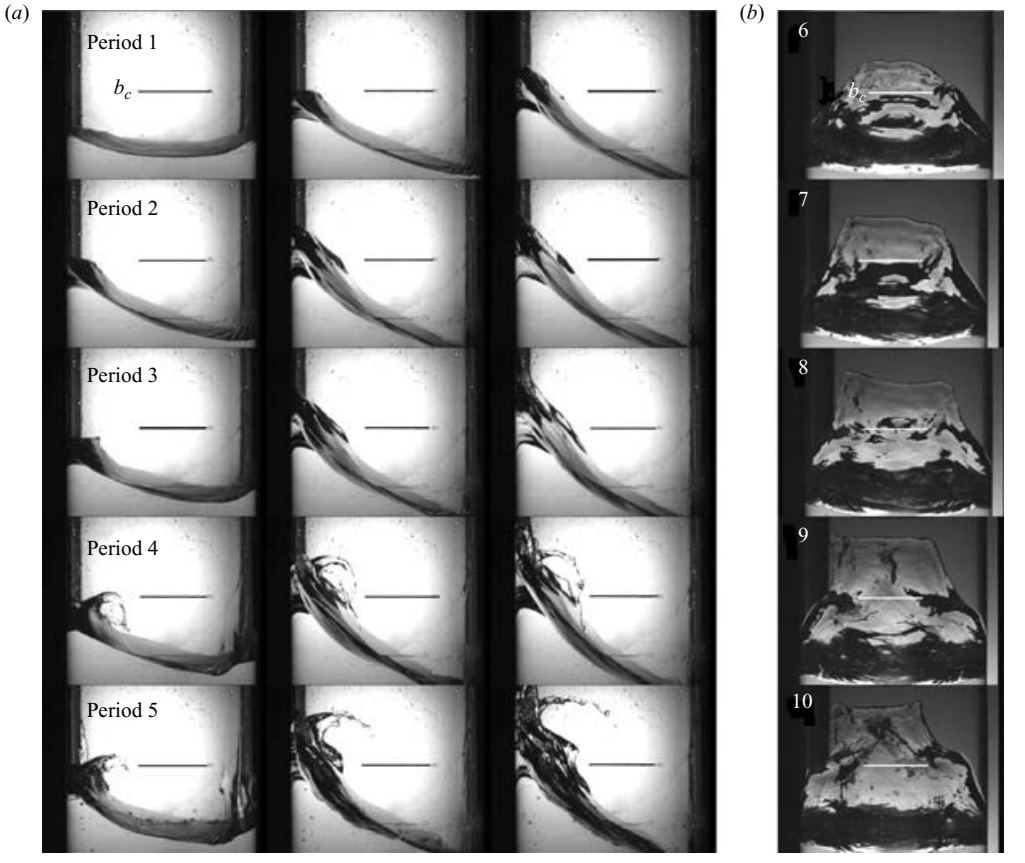


FIGURE 15. (*a*) Sloshing motion viewed perpendicular to the container motion at successive periods. For each period, three images with increasing wave amplitude are shown (*b*), view in the direction of container motion. Cylindrical container of $R = 78$ mm, filled with water to $h/R = 1.5$. The forcing frequency and forcing amplitude are, respectively, $\omega/\omega_1 = 0.96$ and $A_f/R = 0.022$. The wave period is $T = 430$ ms.

to twice the primary frequency ω_1. In § 6.3, where wave breaking in a square-base container is discussed, cross-waves of twice the primary wave frequency are indeed observed, but other scenarios are also possible.

Before the violent wave destabilization (collapse) illustrated in figures 14 and 11, spilling occurs. This is shown in figure 15(*a*) where the motion is viewed perpendicular to the container motion and in figure 15(*b*) aligned with the container motion. The two views are, unfortunately, not simultaneous. In figure 15(*a*) the wave amplitude is shown at five successive periods, starting at $b \approx 1.2b_c$ (period 1) until the wave crest reaches about $1.8b_c$ and spilling occurs (periods 4 and 5). For each period, three images are shown with the wave amplitude increasing from left to right in each row. Figure 15(*b*) corresponds roughly to the maximum wave amplitude (right-hand column of figure 15*a*) viewed from right to left (in the direction of container motion). The images were taken in the container of $R = 78$ mm at forcing frequency and forcing amplitude respectively $\omega/\omega_1 = 0.96$ and $A_f/R = 0.022$.

https://doi.org/10.1017/S0022112007004764 Published online by Cambridge University Press

The mechanism of spilling is analogous to that beautifully demonstrated by Jiang *et al.* (1998) for two-dimensional wave breaking. The relatively thin fluid layer (of thickness $\approx 0.1R$) that, by inertia, is thrown up to a height larger than b_c, moves down by nearly free fall and impinges on the upward moving wave crest during the next oscillation. When the fluid layer falls from a sufficient height, it creates a shoulder on the wave crest that causes the spilling (figure 15*a*, period 4). Bredmose *et al.* (2003) called this wave crest a table-top crest. Their experiments, conducted in a rectangular tank of length to width ratio equal to 3.7, subjected to horizontal forcing, showed the existence of these table-top breakers with long periods of free fall. In the present experiments spilling is not uniform across the wave crest (width of the layer); it is concentrated at the centre and a ligament emerges which breaks up into drops. In two dimensions, the spilling causes sufficient damping that during the next period, the wave amplitude is reduced and the cycle starts again. Jiang *et al.* called it period tripling. In three dimensions, the transverse or crosswise perturbations on the wave crest grow (it starts in image 5 of figure 15*b*) and only after two to three periods is there complete collapse of the wave motion (figures 14 and 11). If the forcing of the container is maintained, the planar wave will start to grow again after a few periods when the irregular sloshing motion has been sufficiently damped. The growth–collapse cycle is quasi-periodic, with the period depending on ω/ω_1 and A_f/R (figure 12).

7. Wave breaking in a square-base container

7.1. *Breaking conditions*

In a square-base container, the span of the wave crest is limited by the sidewalls and is equal to half the primary wavelength. This corresponds to the case mentioned by Taylor (1953) where large-amplitude two-dimensional wave motion is nearly impossible when the standing wave crest is free in the direction of the primary wave motion. In a square-base container, a wall replaces the symmetry plane and stabilizes the wave crest in the direction of the primary wave motion. The container used has a square base of $L = 28$ cm and a depth of 50 cm filled with water or alcohol to $h/L \approx 1$. The forcing amplitude was always $A_f/L = 0.0125$. The dimensionless wavenumber is $k_{ij}L = \pi\sqrt{i^2 + j^2}$ (Faltinsen *et al.* 2003) with natural frequency of the primary, asymmetric modes $\omega_{10}(\pi g/L)^{1/2} = 10.48\ \mathrm{rad\,s^{-1}}$ ($\omega_{10} = \omega_{01} \equiv \omega_1$) and wavelength $\lambda = 2L$. The wave amplitude b_c at which the downward wave acceleration $b\omega^2 = g$ and the wave crest begins to break is $b_c = L/\pi = 0.16\lambda$ (taking $\omega = \omega_1$). This value would be obtained if the wave crest were pointed. Since in reality the wave crest for wave amplitudes $b \leqslant b_c$ is not pointed and is closely approximated by the Penney & Price (1952) relation, the downward acceleration is already equal to g when $b/\lambda = 0.14$. Taylor argued that a fluid particle which rises above $b/\lambda = 0.141$ might experience a downward acceleration larger than g during a small instant of time. He found stable wave motion up to $b/\lambda = 0.14$ with a slight sign of perturbations along the wave crest (crosswise) already beginning at $b/\lambda \approx 0.12$.

Figure 16 shows images of crosswise destabilization of the wave crest in the square-base container. In figure 16(*a*), the temporal growth of this instability is shown during six periods. In figure 16(*b*), the different cross-wave patterns that can be observed are shown. In figure 16(*a*) there is an onset of a short wavelength instability when $b \approx b_c$ (figure 16(*a*)(i)). This instability is compatible with a Rayleigh–Taylor instability assuming a downward acceleration of about $1.1\,g$. This instability is, however, not

https://doi.org/10.1017/S0022112007004764 Published online by Cambridge University Press

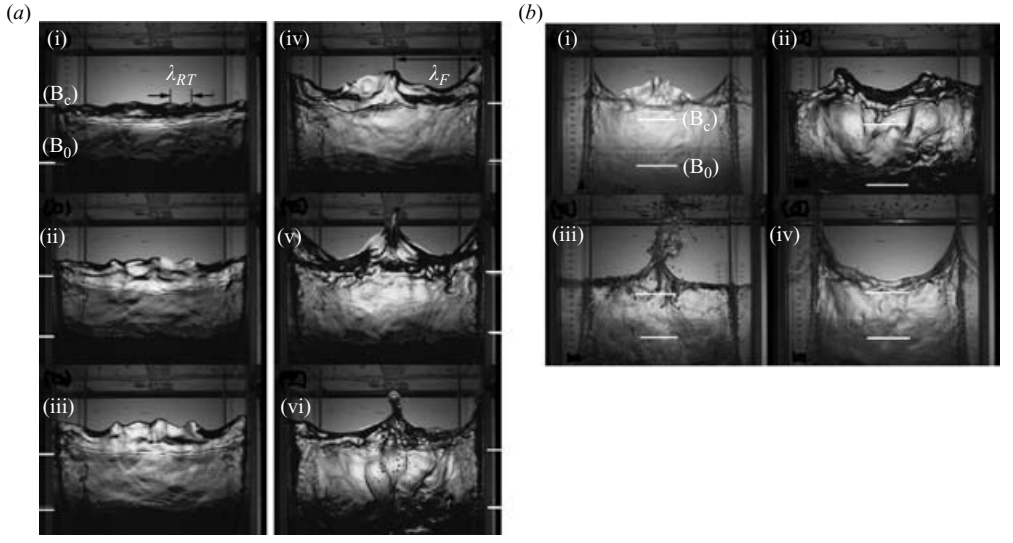


FIGURE 16. Front view of lateral wave profiles in the square-base container. (*a*) Temporal evolution of the crosswise instability of the wave crest; λ_{RT} indicates short-wave instability and λ_F long-wave instability. The fluid is water. (*b*) the four different wave pattern observed. In (*b*), the liquid is alcohol, but patterns are the same as in water; $\omega/\omega_1 = 0.92$, $A_f/L = 0.0125$.

amplified further because the downward acceleration is hardly ever larger than about $1.1g$ and lasts only over a small fraction of the wave period. Measurements showed that at $b = 0.14\lambda$, the downward acceleration is practically equal to g and when $b = 0.24\lambda$ (figure 16(*a*)(iv)) a downward acceleration between g and $1.2\,g$ may exist depending on transverse position. Capillary effects are evaluated to about $0.03\,g$ for water.

In figure 16(*a*) the short wavelength instability (Rayleigh–Taylor instability) is rapidly replaced by instability of wavelength $L/2$ that grows and starts to form conically shaped fluid masses in the centre and at the sidewalls. A ligament emerges from the central conical fluid mass. In figure 16(*b*) three other cross-wave patterns are shown. The pattern in figure 16(*b*)(ii) is the counterpart of figure 16(*b*)(i) with two crests located at $L/4$ from the sidewalls. Figures 2(*b*)(iii) and 2(*b*)(iv) have a wavelength qual to L.

The scenario of wave breaking in a square-base container (figure 17) is very similar to that observed in a cylindrical container (figure 15) except that the crosswise instability of the wave crest is more pronounced. The lumps of fluid above b_c (figure 17*b*) fall freely and impinge on the upward moving wave front during the next oscillation (figure *e*, *f*) producing some splashing (figure 17*f*). As the wave front moves up, a shoulder forms (figure 17*i*) which causes spilling. In figure 17, the cross-wave wavelength is $L/2$ and the frequency is likely to be twice the primary frequency because there is a peak in the centre on one face (figure 16(*b*)(i)) and again a peak on the opposite wall (figure 17*f*, *g*). There is a downward central peak at the wave trough (figure 17*e*) half a period later that would indicate that the cross-wave is in phase with ω_1. The reason for this is most likely the free fall of the fluid lumps that causes the downward central gas entrainment; in figure 17(*f*), the pattern starts to reverse. It was not possible to follow the complete evolution of the cross-wave pattern on one face only to determine without ambiguity its frequency. The scenario shown

https://doi.org/10.1017/S0022112007004764 Published online by Cambridge University Press

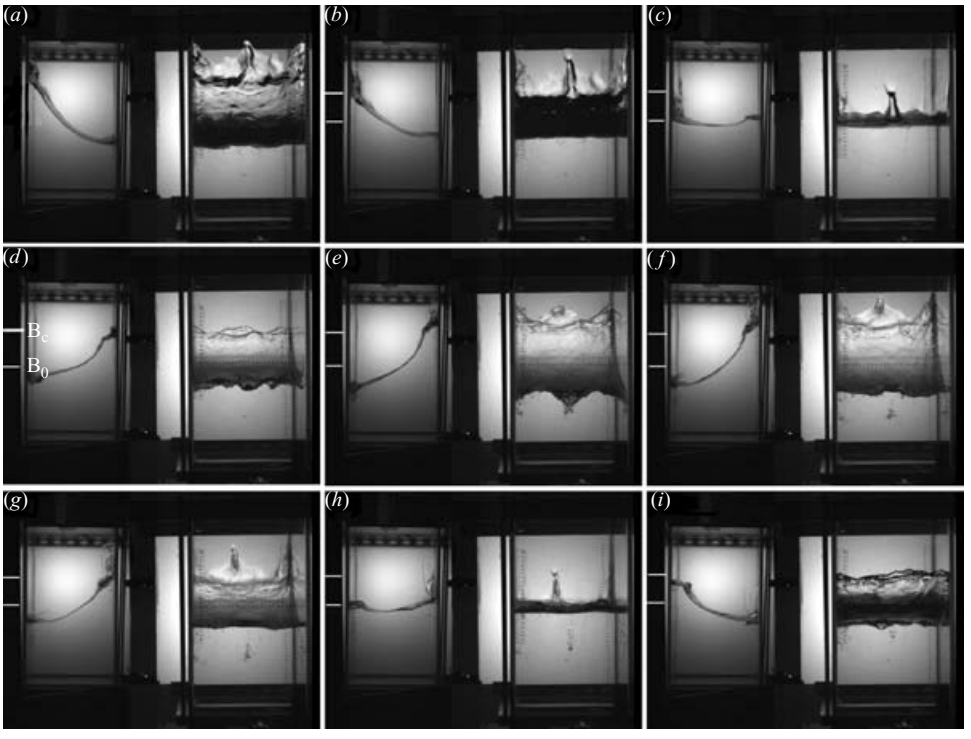


FIGURE 17. Simultaneous front and side views of wave breaking in the square-base container for $\omega/\omega_{11} = 0.97$, $A_f/L = 0.0125$. The fluid is alcohol and the images are taken at a time interval of 66 ms. The wave period is $T = 2\pi/\omega = 617$ ms. The observed pattern corresponds to figure 16(*b*)(i) for which the cross-wave frequency was evaluated as $\omega = 2\omega_1$.

in figure 17 persists for about three to four periods and then the whole wave motion collapses in a way similar to figure 11 because the symmetry is lost and a non-planar irregular motion is generated. Then, the plane wave amplitude starts to grow again. Measurements of the wave heights in a square-base container by Faltinsen *et al.* (2003) demonstrate this growth–collapse cycle.

7.2. *Analysis in terms of parametric instability*

The observed cross-wave instability is most probably of parametric type. The wave motion in the square-base container can be considered analogous to the wave motion generated in a rectangular container of length $2L$ and width L vibrated vertically at frequency $\omega_p = 2\omega_1$, except that in the square-base container, the symmetry plane of the wave crest is replaced by a wall. The tuning and forcing parameters are, respectively (Benjamin & Ursell 1954),

$$p = \frac{4\omega_T^2}{\omega_p^2}, \quad q = 2b_p k_T \tanh(k_T h), \tag{20}$$

where ω_T and k_T are, respectively, the cross-wave frequency and wavenumber. The required vertical vibration amplitude b_p is unknown. Waves of sub-harmonic frequency $\omega_1 = \omega_p/2$ are known to be most unstable. The corresponding wavelength $\lambda = 2L$ is the planar wave motion. However, in the crosswise direction, the wave is bounded by the container width L. A larger forcing amplitude (large forcing parameter) is required to amplify waves of shorter wavelengths (Miles & Henderson

https://doi.org/10.1017/S0022112007004764 Published online by Cambridge University Press

Face 1	Face 2	Wavelength	Frequency
Pattern i	Pattern i	$L/2$	$2\omega_1$
Pattern i	Pattern ii	$L/2$	ω_1
Pattern iii	Pattern iv	L	$2\omega_1$
Pattern iii, then Pattern iv,	Pattern iii then Pattern iv	L	$2\omega_1$

TABLE 1. Likely frequency of the cross-wave patterns shown in figure 16(*b*).

1990), namely $\lambda_T = L$ and $\lambda_T = L/2$ (figure 16). The corresponding values of the tuning parameter are, respectively, $p = 2$ and $p = 4$.

The frequencies of the cross-wave patterns were determined from video images and are given in table 1. In this table, the wave patterns referred to as patterns i, ii, iii, and iv correspond to the images (i), (ii), (iii) and (iv) of figure 16(*b*). The back and front walls at which the wave crests run up successively are, respectively, referred to as face 1 and face 2. The synchronous behaviour $\omega_T = 2\omega_1$ is compatible with classical parametric instability when the tuning parameter $p = 4$, (20). This wavelength corresponds also to the secondary mode $2\omega_1$ which is amplified by the quadratic terms of the primary modes, (11). The wavelengths L of rows 3 and 4 of table 1, would correspond to $p = 2$ if the frequency were $\omega_T = \sqrt{2}\omega_1$. In a square-base container this frequency corresponds to the second natural frequency $\omega_{20} = \sqrt{2}\omega_1$. It is possible that there is an interaction between the primary modes of ω_1 and secondary modes of $2\omega_1$ that allow the wavelength L to exist. The behaviour of row 2 is unexplained.

8. Conclusions

The aims of the experiments on sloshing in circular and square-base cylindrical containers of primary natural frequency ω_1, subjected to harmonic horizontal forcing of frequencies near ω_1 and forcing amplitude A_f, were twofold: (i) to determine the bounds of existence of the different wave regimes and (ii), to clarify the transients from planar waves to swirl wave and from planar and swirl waves to chaos including wave breaking. Only large fluid depth, $h/R > 1$, was considered such that the amplitude–frequency response is independent of fluid depth. The liquids used (water and alcohol) were low-viscosity liquids and satisfy the conditions of small damping, $\alpha^2 \ll 1$. Because of deep-water conditions, the nonlinearity of planar wave resonance is negative (Miles 1984*a*) with the boundary of transition from steady-state planar waves to chaos and wave breaking depending critically on excitation amplitude. The non-planar wave mode (swirl) is situated near and above the natural frequency. Its bounds have been clarified and compared with Miles' (1984*b*) weakly non-linear theory. The amplitude response of planar waves is in good agreement with Miles' theory. When $\omega > \omega_1$, planar waves bifurcate to a swirl wave at a finite wave amplitude, the value of which depends on forcing amplitude and frequency. The swirl wave amplitude grows exponentially and saturates at a certain value. The swirl wave response has a hard-spring behaviour, is very robust and generates a vortical flow of the fluid column which, by the Doppler shift, allows the swirling wave to remain stable up to relatively large excitation frequencies. At collapse of the swirl, the phase lag is close to $-\pi/2$, followed by planar out-of-phase wave motion. When $\omega < \omega_1$, planar waves bifurcate to

https://doi.org/10.1017/S0022112007004764 Published online by Cambridge University Press

chaotic sloshing if, for a given forcing amplitude, the dimensionless forcing frequency ω/ω_1 is increased beyond the stability bound (turning point). The temporal increase in wave amplitude of these resonant waves depends strongly on forcing amplitude. These waves remain stable up to an amplitude of $b/R \cong 0.54$ where the downward wave crest acceleration is equal to or slightly larger than gravity. Beyond this wave amplitude, a liquid layer is projected up the wall. Depending on forcing amplitude and forcing frequency, the maximum height reached by the leading edge of this layer is nearly twice the stable wave amplitude. Wave breaking and following wave motion collapse with irregular non-planar sloshing, limits the maximum height. As the wave amplitude grows, the phase lag increases and is about $-\pi$ at collapse of the wave motion. Near the bifurcation point β_2, that is, in close vicinity of the natural frequency, chaotic wave motion exists without wave breaking (see figure 12*a*).

Chaotic wave motions and wave breaking occur quasi-periodically, starting with the growth of planar wave amplitude followed, generally by breaking (except near β_2) and irregular sloshing. Then, after sufficient damping of the irregular sloshing motion, the amplitude of planar wave motion grows again. The maximum amplitude reached before collapse and the periodicity of the growth–collapse–irregular swirl–growth depend on forcing amplitude and forcing frequency. Breaking starts, in general, with a pointed crest consisting of a layer that moves up the wall. This layer then moves downward by nearly free fall and lags behind the wave motion so that it impinges on the upward moving wavefront during the next oscillation. This causes spilling owing to the encounter of this downward moving fluid layer with the upward moving wave crest. This spilling process is repeated over two to three periods and then the resulting strong perturbations cause the wave motion to collapse. The following fluid motion is very irregular, probably turbulent, with strong (bulk) damping, allowing renewed growth of planar wave motion. In two dimensions, the spilling process is similar, as was demonstrated by Jiang *et al.* (1998), except that after one spilling event the associated dissipation leads to a stable wave in the next cycle. This process was referred to as period-tripled breaking. In three dimensions, because of the destabilization of the wave crest in the crosswise direction, spilling is not uniform along the wave crest. For this reason, free fall of fluid lumps and spilling can be repeated over a few wave periods before perturbations become large enough to generate fully three-dimensional motion (figure 14).

The complementary experiments conducted in the square-base container of base dimension L, allowed the wave crest destabilization to be investigated in more detail. Four different cross-wave patterns of wavelengths L and $L/2$ have been identified with frequencies equal to ω_1 and probably also $2\omega_1$. This cross-wave instability is interpreted in terms of parametric instability. The cross-wave instability can develop into ligaments and drop ejection. The size of the drops depends on the surface tension of the liquid, but the cross-wave pattern does not seem to be influenced by surface tension.

The results obtained in two containers, which differ in size, by a factor of two are, as expected, identical in dimensionless terms. Therefore, the up-scaling of the results to large containers, encountered in application, is possible. It requires geometric similarity as well as similarity of the frequency-offset parameter β composed of the dimensionless forcing amplitude A_f/R and dimensionless forcing frequency ω/ω_1. For the same value of β, the growth rates of the wave amplitude of planar and unstable waves in the chaotic regime is practically linear in time and depends on forcing amplitude $(A_f/R)^n$ (19) with $n \sim 1$. The liquid depth h/R is a further important parameter unless conditions of deep-water waves are satisfied as in the present

https://doi.org/10.1017/S0022112007004764 Published online by Cambridge University Press

experiments. The fluid properties must satisfy the conditions of small damping, $\alpha^2 \ll 1$, and small effects of surface tension (Bond number $Bo = \rho g R^2/\sigma \gg 1$). Surface tension effects however, play, a role in the final stage of wave breaking (drop formation).

This work was financially supported by contract CNES 5866 within the frame of the French–German program COMPERE. A.-R. L. acknowledges a CNES-CNRS PhD research fellowship. The authors wish to thank Pierre Carecchio and Joseph Virone for their technical help.

REFERENCES

Abramson, H. N. (Ed.) 1966 The dynamic behavior of liquids in moving containers. *NASA TR* SP-106.

Abramson, H. N., Chu, W. H. & Dodge, F. T. 1966 Nonlinear effects in lateral sloshing. In *The Dynamic Behaviour of Liquids in Moving Containers* (ed. H. N. Abramson). *NASA TR* SP-106, 79–103.

Benjamin, T. B. & Ursell, F. 1954 The stability of the plane free surface of a liquid in vertical periodic motion. *Proc. R. Soc. Lond.* A, **225**, 505–515.

Bredmose, H., Brocchini, M., Peregrine, D. H. & Thais, L. 2003 Experimental investigation and numerical modelling of steep forced water waves. *J. Fluid Mech.* **490**, 217–249.

Bridges, T. J. 1987 Secondary bifurcation and change of type for three-dimensional standing waves in finite depth. *J. Fluid Mech.* **179**, 137–153.

Faller, A. J. 1983 The generation of swirl in a circular cylinder by rotillation. Part 2: Theory of rotillation wave and boundary-layer pumping. *Tech. Rep.* BN-998, University of Maryland, USA.

Faller, A. J. 2001 The constant-V vortex. *J. Fluid Mech.* **434**, 167–180.

Faltinsen, O. M., Rognebakke, O. F., Lukovsky, I. A. & Timokha, A. N. 2000 Multidimensional modal analysis of nonlinear sloshing in rectangular tank with finite water depth. *J. Fluid Mech.* **407**, 201–234.

Faltinsen, O. M., Rognebakke, O. F. & Timokha, A. N. 2003 Resonant three-dimensional nonlinear sloshing in a square basin. *J. Fluid Mech.* **487**, 1–42.

Faltinsen, O. M., Rognebakke, O. F. & Timokha, A. N. 2005 Classification of three-dimensional nonlinear sloshing in square-base tank with finite depth. *J. Fluids Struct.* **20**, 81–103.

Faltinsen, O. M., Rognebakke, O. F. & Timokha, A. N. 2006 Transient and steady-state amplitudes of resonant three-dimensional sloshing in a square base tank with finite fluid depth. *Phys. Fluids*, **18**, 012103-1–012103-14.

Funakoshi, M. & Inoue, S. 1988 Surface waves due to resonant horizontal oscillations. *J. Fluid Mech.* **192**, 219–247.

Gavrilyuk, I., Lukovsky, I. & Timokha, A. N. 2000 A multimodal approach to nonlinear sloshing in a circular tank. *Hybrid Meth. in Engng* **2**, 463–483.

Henderson, D. M. & Miles, J. W. 1990 Single-mode Faraday waves in small containers. *J. Fluid Mech.* **213**, 95–109.

Hutton, R. E. 1963 An investigation of resonant nonlinear non-planar free surface oscillations of a fluid. *NASA TN* D-1870.

Hutton, R. E. 1964 Fluid–particle motion during rotary sloshing. *Trans. ASME* E: *J. Appl. Mech.* **31-1**, 123–130.

Ibrahim, R. A. 2005 *Liquid Sloshing Dynamics*. Cambridge University Press.

James, A. J., Smith, M. K. & Glezer, A. 2003 Vibration-induced drop atomization and the numerical simulation of low-frequency single-drop ejection. *J. Fluid Mech.* **476**, 29–62.

Jiang, L., Perlin, M. & Schultz, W. W. 1998 Period tripling and energy dissipation of breaking standing waves. *J. Fluid Mech.* **369**, 273–299.

Lighthill, J. 1978 *Waves in Fluids*. Cambridge University Press.

Miles, J. W. 1976 Nonlinear surface waves in closed basins. *J. Fluid Mech.* **75**, 419–448.

Miles, J. W. 1984*a* Internally resonant surface waves in a circular cylinder. *J. Fluid Mech.* **149**, 1–14.

Miles, J. W. 1984*b* Resonantly forced surface waves in a circular cylinder. *J. Fluid Mech.* **149**, 15–31.

https://doi.org/10.1017/S0022112007004764 Published online by Cambridge University Press

Miles, J. W. 1984*c* Resonant motion of a spherical pendulum. *Physica* **11**D, 309–323.

Miles, J. W. & Henderson D. M. 1990 Parametrically forced surface waves. *Annu. Rev. Fluid Mech.* **22**, 143–165.

Miles, J. W. & Henderson D. M. 1998 A note on interior vs. boundary-layer damping of surface waves in a circular cylinder. *J. Fluid Mech.* **364**, 319–323.

Penney, W. G. & Price, A. T. 1952 Part ii: finite periodic stationary gravity waves in a perfect liquid. *Phil. Trans. R. Soc. Lond.* A **244**, 254–284.

Prandtl, L. 1949 Erzeugung von Zirkulationen beim Schutten von Gefassen. *Z. Angew. Math. Mech.* **29**, 8–9.

Royon-Lebeaud, A. 2005 Ballottement des liquids dans les reservoirs cylindriques soumis à une oscillation harmonique Thèse de l'UJF, Grenoble (http://tel.ccsd.cnrs.fr).

Silverman, S. & Abramson, H. N. 1966 Damping of liquid motions and lateral sloshing. In *The Dynamic Behaviour of Liquids in Moving Container* (ed. H. N. Abramson). *NASA TR* SP-106, 105–143.

Taylor, G. I. 1953 An experimental study of standing waves. *Phil. Trans. R. Soc.* 44–59.

Waterhouse, D. D. 1994 Resonant sloshing near a critical depth. *J. Fluid Mech.* **281**, 313–318.

https://doi.org/10.1017/S0022112007004764 Published online by Cambridge University Press